Biological and physical controls on N_2, O_2 and CO_2 distributions in contrasting Southern Ocean surface waters

Philippe D. Tortell[1,2], Henry C. Bittig[3], Arne Körtzinger[3], Elizabeth M. Jones[4], and Mario Hoppema[4]

[1]Department of Earth, Ocean and Atmospheric Sciences, University of British Columbia, 2207 Main Mall, Vancouver BC, Canada, V6T 1Z4. ptortell@eos.ubc.ca

[2]Department of Botany, University of British Columbia, 6270 University Blvd., Vancouver BC, Canada, V6T 1Z4

[3]Marine Biogeochemistry, GEOMAR Helmholtz Centre for Ocean Research Kiel, Düsternbrooker Weg 20, 24105 Kiel, Germany

[4]Alfred Wegener Institute, Helmholtz Centre for Polar and Marine Research, Postfach 120161, 27515 Bremerhaven, Germany

Corresponding Author: Philippe D. Tortell, Dept. of Earth, Ocean and Atmospheric Sciences, University of British Columbia, 2207 Main Mall, Vancouver BC, Canada, V6T 1Z4. (ptortell@eos.ubc.ca)

Key Points:

- Biological and physical controls on Southern Ocean gases are quantified
- Sea-air CO_2 fluxes significantly exceed regional climatological values
- Net community production estimates are corrected for physical processes

Abstract:

We present measurements of pCO_2, O_2 concentration, biological oxygen saturation ($\Delta O_2/Ar$) and N_2 saturation (ΔN_2) in Southern Ocean surface waters during austral summer, 2010–2011. Phytoplankton biomass varied strongly across distinct hydrographic zones, with high chlorophyll *a* (Chla) concentrations in regions of frontal mixing and sea-ice melt. pCO_2 and ΔO_2 /Ar exhibited large spatial gradients (range 90 to 450 μatm and -10 to 60%, respectively) and co-varied strongly with Chla. However, the ratio of biological O_2 accumulation to dissolved inorganic carbon (DIC) drawdown was significantly lower than expected from photosynthetic stoichiometry, reflecting the differential time-scales of O_2 and CO_2 air-sea equilibration. We measured significant oceanic CO_2 uptake, with a mean air-sea flux (~ -10 mmol m^{-2} d^{-1}) that significantly exceeded regional climatological values. N_2 was mostly supersaturated in surface waters (mean ΔN_2 of +2.5 %), while physical processes resulted in both supersaturation and undersaturation of mixed layer O_2 (mean ΔO_{2phys} = 2.1 %). Box model calculations were able to reproduce much of the spatial variability of ΔN_2 and ΔO_{2phys} along the cruise track, demonstrating significant effects of air-sea exchange processes (*e.g.* atmospheric pressure changes and bubble injection) and mixed layer entrainment on surface gas disequilibria. Net community production (NCP) derived from entrainment-corrected surface ΔO_2 /Ar data, ranged from ~ -40 to > 300 mmol O_2 m^{-2} d^{-1} and showed good coherence with independent NCP estimates based on seasonal mixed layer DIC deficits. Elevated NCP was observed in hydrographic frontal zones and stratified regions of sea-ice melt, reflecting physical controls on surface water light fields and nutrient availability.

1. Introduction:

The Southern Ocean plays a key role in global nutrient and carbon cycles [*Sarmiento et al.*, 2004; *Schlitzer*, 2002]. This vast region contributes significantly to oceanic CO_2 uptake through the vertical export of particulate organic carbon [*Honjo et al.*, 2008; *Schlitzer*, 2002; *Trull et al.*, 2001], and the subduction of CO_2-rich polar water masses into the ocean interior [*Caldeira and Duffy*, 2000; *Sarmiento and Toggweiler*, 1984]. These biological and physical carbon pumps also transport oxygen and macro-nutrients into the low latitudes, where they influence biological productivity over large spatial scales [*Marinov et al.*, 2006; *Sarmiento et al.*, 2004]. In the off-shore pelagic realm, Southern Ocean primary production and biological CO_2 uptake appear to be controlled by a combination of light and iron limitation [*Boyd*, 2002]. Large scale patterns of aeolian iron deposition have been linked to spatial gradients in surface water productivity [*Cassar et al.*, 2007], while vertical mixing at frontal zones has been shown to drive mesoscale and sub-mesoscale biological gradients [*Sokolov and Rintoul*, 2007]. Relative to the open ocean, field data are sparse over much of the Antarctic continental shelf and marginal ice zone (MIZ), where productivity is influenced by iron input from sediments [*Coale et al.*, 2005; *Planquette et al.*, 2013] and melting ice [*Gerringa et al.*, 2012; *Sedwick and DiTullio*, 1997], and by large seasonal cycles in solar irradiance, mixed layer depth and sea ice cover [*Arrigo and van Dijken*, 2003]. Although these high latitude regions contribute disproportionately (on an areal basis) to Southern Ocean nutrient and carbon cycles [*Arrigo et al.*, 2008], their biological and physical dynamics remain poorly described.

Here we present new results from a two-month survey of surface hydrography and dissolved gas concentrations across the Atlantic sector of the Southern Ocean and the region west of the Antarctic Peninsula. We use our observations to characterize the spatial variability of surface gases in contrasting Southern Ocean regions (offshore pelagic, continental shelf and MIZ), and to examine the relative influence of physical *vs.* biological controls on biogeochemical processes. The interplay of physical and biological forcing is particularly important in determining surface water pCO_2 and O_2 distributions. Net community production (NCP, *i.e.* gross photosynthesis minus community respiration) leads to CO_2 drawdown (*i.e.* decreased pCO_2) in the mixed layer, coupled with biologically-induced O_2 supersaturation [*Carrillo et al.*, 2004]. NCP is sensitive to physical factors (*e.g.* wind speed, solar irradiance and ice cover) that control nutrient supply and

mixed layer light intensity. Physical processes also influence surface O_2 and CO_2 by modulating the strength of diffusive air-sea exchange, which acts to restore gas concentrations back to atmospheric equilibrium, and bubble processes, which lead to supersaturation of surface water gases [*Keeling*, 1993]. Due to chemical buffering of the inorganic C system in seawater, the diffusive air-sea equilibration time scale is typically ~ 10-fold slower for CO_2 than for O_2 [*Sarmiento and Gruber*, 2006], and gas exchange can thus overprint the biological production signal, shifting the $pCO_2 - O_2$ relationship away from photosynthetic stoichiometry [*Körtzinger et al.*, 2008].

Changes in surface water temperature and salinity can also influence O_2 and CO_2 distributions through their effect on gas solubility. For O_2, these thermodynamic effects can be removed by normalization to argon, a biologically inert gas with solubility properties that are virtually identical to O_2. The O_2 /Ar ratio thus serves as a specific tracer for biological O_2 cycling [*Craig and Hayward*, 1987], and recent field measurements of O_2/Ar disequilibrium (ΔO_2/Ar) have been used to map the large-scale spatial distribution of NCP in Southern Ocean surface waters [*Cassar et al.*, 2011; *Castro-Morales et al.*, 2013; *Reuer et al.*, 2007; *Shadwick et al.*, 2014; *Tortell and Long*, 2009]. NCP estimates derived from ΔO_2/Ar measurements are based on a steady-state mixed layer model [*Kaiser et al.*, 2005; *Reuer et al.*, 2007], where vertical and lateral exchange of O_2 into the mixed layer is assumed to be negligible and NCP can thus be equated to the biologically induced sea-air flux of O_2 (O_2-bioflux). These assumptions are likely invalid over significant portions of the Southern Ocean, where vertical entrainment of biologically modified sub-surface waters leads to significant uncertainty in derived mixed layer NCP values [*Jonsson et al.*, 2013]. Better constraints on the physical contributions to mixed layer O_2 mass balance are thus needed to improve the use of ΔO_2/Ar as a productivity tracer.

Like Ar, N_2 is biologically inert in the Southern Ocean, where nitrogen fixation and denitrification are inhibited by high NO_3^- and O_2 concentrations, respectively. Given the high atmospheric concentrations of N_2 and its relatively low solubility in seawater, this gas provides a useful tracer for air-sea exchange processes, including bubble injection [*Schudlich and Emerson*, 1996]. A number of studies have used surface ocean N_2 disequilibrium measurements (ΔN_2) to examine air-sea exchange [*Emerson et al.*, 2002; *Hamme and Emerson*, 2006; *Vagle et al.*, 2010], and a mechanistic framework has recently been developed to quantitatively interpret surface N_2 data [*Liang et al.*, 2013; *Nicholson et al.*, 2008; *Nicholson et al.*, 2011; *Stanley et al.*,

2009]. At present, we are aware of only one published ΔN_2 data set from Southern Ocean waters [*Weeding and Trull*, 2014]. Additional ΔN_2 measurements from this region are thus needed to validate the model-based calculations under conditions of high wind-speeds, strong gradients in atmospheric pressure and significant bubble injection fluxes.

Using simultaneous measurements of N_2, O_2, ΔO_2/Ar and CO_2, in combination with ancillary data and box model calculations, we examined the dominant controls on surface gas saturation states in contrasting Southern Ocean surface waters. Our results provide insight into the factors driving gas dynamics in various sub-regions of the Southern Ocean, demonstrating clear regional differences in the relative importance of physical and biological forcing. Our observations reveal strong biological controls on surface CO_2 and O_2 distributions, with a significant imprint of air-sea exchange. Using box model calculations, we show that the formulation of Nicholson et al. [2011] is able to provide reasonable estimates of physically-induced changes in O_2 and N_2 saturation states, and we derive NCP estimates that are corrected for entrainment of biologically modified sub-surface waters into the mixed layer. Our work builds on the recent study of Shadwick et al. [2014] examining CO_2, O_2 and ΔO_2 /Ar along a transect south of Australia, and Weeding and Trull [2014], who present a mooring-based O_2 and N_2 time-series for the Subantarctic region south of Tasmania. To our knowledge, our work represents the first simultaneous measurements of pCO_2, ΔO_2, ΔO_2 /Ar and ΔN_2 for the Southern Ocean, and we show how these combined observations can provide powerful insights into surface water biogeochemical processes across a range of hydrographic regimes.

2. Methods:

2.1 Study site and hydrographic measurements

We conducted a 10-week survey of Southern Ocean waters from Nov. 29, 2010 to Feb. 3, 2011 on board the research vessel Polarstern (cruise ANT-XXVII/2; [*Rohardt*, 2011]). Our cruise track from Cape Town, South Africa, to Punta Arenas, Chile (Figure 1) encompassed a number of distinct hydrographic regimes. For the purposes of our analysis, we separate the cruise track into three sub-regions. We first sampled a N-S transect ~ 40˚S to 70˚S, crossing a number of prominent hydrographic fronts [*Orsi et al.*, 1995], including the Subtropical Front

(STF), Sub-Antarctic Front (SAF), Polar Front (PF), Southern Antarctic Circumpolar Current Front (SACCF) and Southern Boundary of the Antarctic Circumpolar Current (SBdy). We then followed an E-W transect along the outer edge of the Weddell Sea MIZ, and conducted an intensive survey of the West Antarctic Peninsula (WAP) along the Palmer Long Term Ecological Research (LTER) sampling grid [*Waters and Smith*, 1992].

Sea surface temperature (SST) and salinity (SSS) were measured continuously along the cruise track using an on-board thermosalinograph (TSG; Sea-Bird Electronics, model SBE-21) sampling from an uncontaminated seawater supply with a nominal intake depth of 11 m. Daily calibrations of the TSG salinity measurements were conducted using discrete samples analyzed on a salinometer (Optimare GmbH, Precision Salinometer). Sea surface Chla fluorescence, used as a proxy for bulk phytoplankton biomass, was continuously measured by the ship's underway fluorometer (WET labs, ECO). The fluorometer data were not calibrated to absolute Chla concentrations and are thus used here only as a relative measure of total phytoplankton abundance. Some day-time non-photochemical quenching of Chla fluorescence is expected, independent of changes in phytoplankton biomass.

Depth profiles of seawater potential temperature, salinity and Chla fluorescence were obtained from CTD casts at 188 stations along the cruise track. Temperature and conductivity were measured with Sea-Bird SBE3plus and SBE4 sensors, respectively, while Chla fluorescence was measured with a WET labs ECO fluorometer. Temperature and salinity profiles were used to define the mixed layer depth for each station based on the curvature of near surface layer density or temperature profiles as described by Lorbacher et al. [2006]. Mixed layer temperature and salinity data derived from CTD casts showed very good agreement with surface TSG data (mean offset of −0.078 ˚C and −0.01, respectively). The concentration of O_2 in depth profiles was measured using a CTD-mounted Sea-Bird SBE43 sensor. The CTD O_2 sensor was calibrated using Winkler titrations of discrete samples, with visual endpoint determination using a starch indicator (precision of 0.3 μmol L^{-1}) and KIO_3 standardization of the thiosulfate titration solutions [*Dickson*, 1994]. All of the CTD sensors were sent to the manufacturer for calibration prior to and immediately after the cruise. Full quality-controlled hydrographic data from the cruise are available in the Pangaea database (www.pangaea.de).

2.2 Surface water gas measurements

Surface pCO_2 and O_2 /Ar ratios were measured every ~ 30 s from the keel intake supply using membrane inlet mass spectrometry (MIMS), following the protocols described by Tortell et al. [2011]. At typical cruising speeds of 8–10 knots, this sampling frequency translates into one measurement every ~ 200 m along the cruise track. The pCO_2 measurements were calibrated using temperature-controlled seawater standards [*Tortell et al.*, 2011], and the resulting pCO_2 data were corrected to in situ SST following [*Takahashi et al.*, 2002]. Note that pCO_2 data are not available for much of the N-S transect due to instrument problems. O_2 /Ar measurements in the flow-through seawater, $(O_2/Ar)_{meas}$, were normalized to values measured every few hours in air-equilibrated, temperature-controlled seawater standards, $(O_2/Ar)_{sat.}$ [*Tortell et al.*, 2011], to derive a biological O_2 saturation term, ΔO_2 /Ar, expressed in % deviation from equilibrium.

This term was calculated as [*Craig and Hayward*, 1987]:

$$\Delta O_2/Ar = [(O_2/Ar)_{meas} / (O_2/Ar)_{sat} - 1] * 100 \quad (1)$$

Surface O_2 concentration measurements were made using an optode (Aanderaa Data Instruments, model 3830), while total gas pressure (mbar) was measured using a gas tension device (Pro-Oceanus, model HGTD). The gas tension device was not functional during the latter half of the cruise. Both the optode and HGTD were submerged in a thermally insulated flow-through box connected to the keel seawater intake supply, and set to acquire data with a 1 min resolution (close to the response time of the HGTD). The optode O_2 measurements were calibrated against CTD-O_2 data, and cross validated against discrete Winkler titrations. The O_2 saturation state (ΔO_2; % deviation from equilibrium) was derived from measured O_2 concentrations and an equilibrium O_2 concentration computed from surface water temperature, salinity and atmospheric pressure with the solubility function of Garcia & Gordon [1992]. Using our optode and MIMS data, we derived an estimate of the physical contribution to O_2 disequilibria in surface waters, ΔO_{2phys}.

$$\Delta O_{2phys} = \Delta O_{2optode} - \Delta O_2/Ar_{MIMS} \quad (2)$$

The rationale for this approach is that optode-based ΔO_2 is sensitive to both physical and biological influences, whereas MIMS-based ΔO_2 /Ar reflects only the biological contribution to

O_2 disequilibria [*Craig and Hayward*, 1987], after normalizing for physical effects using the biologically inert analog, argon. As calculated here (2), ΔO_{2phys} is thus functionally equivalent to the physically-induced changes in Argon saturation, ΔAr.

Following the approach of McNeil et al. [*McNeil et al.*, 2005; *McNeil et al.*, 1995], we derived estimates of N_2 partial pressure from GTD total gas pressure by subtracting the partial pressures of O_2 (derived from optode measurements), water vapour (calculated from SST and SSS) and Ar.

$$pN_2 \approx p\text{Total} - pO_2 - pH_2O - p\text{Ar} \quad (3)$$

In previous studies, seawater Ar concentrations have been assumed to be at atmospheric equilibrium values. This assumption contributes only a small uncertainty (< 0.1%) to the calculation of N_2 concentrations [*McNeil et al.*, 1995], since Ar is a minor constituent of total partial pressure and varies by only a few percent. Indeed, we observed a negligible difference between pN_2 calculated assuming 100% Ar saturation and calculations that included a specific ΔAr term (derived from ΔO_{2phys}). Similarly, the inclusion of pCO_2 into the calculation did not have a significant effect on the resulting pN_2. The N_2 saturation state (ΔN_2) was calculated from GTD-derived N_2 concentrations and observed atmospheric pressure using the SST and salinity-dependent N_2 solubility constant of Hamme and Emmerson [2004].

2.3 Ancillary data

Ancillary meteorological and oceanographic data from a number of sources were used to provide a broader environmental context for our observations, and input data for model calculations (see below). Instantaneous measurements of sea level atmospheric pressure, wind speed (corrected to 10 m above sea level) and solar irradiance were obtained from weather station sensors on board the research vessel. Additional synoptic data on wind speed, sea level atmospheric pressure and humidity were obtained from the NCEP reanalysis (http://www.esrl.noaa.gov/psd/data/reanalysis/reanalysis.shtml) at 2.5˚ and 6 h resolution, while regional SST information was derived from NOAA OISST (http://www.ncdc.noaa.gov/sst/) at 0.25˚ and 24 h resolution. The NCEP wind speed data showed reasonably good agreement with

the instantaneous ship-board measurements (r = 0.78, RMSE = 2.9 m s^{-1}). Although there was a slight offset towards lower wind speeds in the NCEP data, the mean difference (-0.94 m s^{-1} ± 3.11) was not significantly different from zero. Sea ice data (% cover) at 3 km and 24 h resolution were derived from AMSR-E satellite imagery using the ASI re-processing algorithm provided by the Institute of Environmental Physics at the University of Bremen, Germany [*Spreen et al.*, 2008]. Regional sea surface salinity was obtained from the Mercator global operational system PSY3V3 model at 0.25˚ and 24 h resolution (http://www.mercator-ocean.fr/eng/produits-services/Reference-products#tps_differe). Surface Chla concentrations were obtained from Level 3 AquaModis satellite data (http://oceancolor.gsfc.nasa.gov/cgi/l3). We used 9 km resolution imagery, with 8-day composite data linearly interpolated to daily values.

2.4 CO_2 flux calculations

Surface gas measurements and wind-speed data were used to derive sea-air flux estimates for CO_2. The CO_2 fluxes were calculated as:

$$F_{CO_2} = k_{CO_2}\, \alpha_{CO_2}\, (pCO_{2sw} - pCO_{2atm})\, (1 - A)^{0.4} \quad (4)$$

where k_{CO_2} is the gas transfer velocity (m d^{-1}), calculated from wind speed data and the temperature-dependent Schmidt number using the parameterization of Sweeney et al. [2007], α_{CO_2} is the temperature and salinity-dependent solubility of CO_2 [*Weiss*, 1974] and A is the fraction of sea surface covered by ice. The exponential term used to scale gas exchange as a function of ice cover is derived from Loose et al. [2009]. For these flux calculations, we used an atmospheric CO_2 mole fraction of 396 ppmv, derived from the GlobalView pCO_2 data (www.esrl.noaa.gov/gmd/ccgg/globalview/; 60˚S to 70˚S, Dec. 2010 - Feb. 2011), corrected to 100% humidity at SST and SSS and the atmospheric pressure derived from ship-based sensors. Wind speeds used for the flux calculations were derived from one week averages of the NCEP reanalysis product, matched to the ship's position along the cruise track.

2.5 Carbonate system measurements and calculations

Discrete samples for carbonate system measurements were collected at selected stations along the cruise track using 12 L Niskin bottles mounted on the CTD rosette. Total alkalinity was measured using potentiometric gran titration [*Brewer et al.*, 1986], calibrated against certified reference material (batches 100 and 105) supplied by Dr. Andrew Dickson, Scripps Institution of Oceanography [*Dickson et al.*, 2007]. The precision of the alkalinity measurements was 1.5 μmol kg^{-1}. Seawater (500 mL) for DIC analysis was collected in borosilicate glass bottles and analysed within 20 hours using a VINDTA 3C instrument (Versatile INstrument for the Determination of Total Alkalinity, Marianda, Kiel). The DIC concentration was determined by coulometric analysis [*Johnson et al.*, 1987], with calibration against certified reference materials (CRM, batches 100 and 105) performed at the start and end of each measurement cycle. The precision of the DIC measurements was 1.0 μmol kg^{-1}, based on the average difference between all CRM in-bottle duplicate analyses (n = 87), and the accuracy was estimated as 2.0 μmol kg^{-1}.

Depth-integrated DIC deficits were calculated from vertical profiles relative to the concentration at the depth of the potential temperature minimum, representing the Winter Water. The depth of the potential temperature minimum was determined from the CTD profiles. Vertical integration to the potential temperature minimum was used to derive the chemical deficits in the summer surface layer. DIC data were normalized to average Winter Water salinity (34.2, n = 105) to account for dilution through addition of sea ice melt water. The chemical deficits, calculated in this way, represent the time-integrated change of the surface ocean since the end of the winter. This technique assumes that DIC concentrations at the potential temperature minimum represent the winter reference with no significant lateral or vertical exchange. This assumption has been used in prior studies [*Hoppema et al.*, 2007; *Jennings et al.*, 1984; *Rubin et al.*, 1998] and appears to be reasonably robust for the Weddell Sea [*Hoppema et al.*, 2000b].

In order to obtain high spatial resolution surface carbonate system data along the cruise track, we derived an empirical linear relationship between salinity and alkalinity along the E-W and WAP transects (n = 2098, $r^2 > 0.85$, root mean square error = 6.1 μmol kg^{-1}), and used this relationship to compute alkalinity from thermosalinograph salinity measurements. Total dissolved inorganic carbon (DIC) along the cruise track was then computed from measured pCO_2

and the derived alkalinity using CO2SYS [*Pierrot et al.*, 2006], with the equilibrium constants of Mehrbach et al., [1973] refit by Dickson and Millero [1987]. For the WAP and Weddell regions, the root mean square error of the DIC estimates derived from this analysis was 7.1 and 3.8 μmol kg^{-1}, respectively. This error term was based on a comparison of DIC values obtained using measured vs. empirically-derived alkalinity.

2.6 Box model calculations

Following the work of Emerson et al. [2008] and Nicholson et al. [2011], we used a simple box model to assess the physical contributions to N_2 and O_2 disequilibria in the mixed layer. The 1-D model includes an air-sea gas exchange term, F_{as} and a sub-surface water entrainment term, F_{entr}, associated with mixed layer deepening events. Lateral and vertical advection, and vertical diffusive mixing were assumed to be negligible, and no biological production / consumption term was included in order to isolate physical forcing. For a given gas, x, the change in mixed layer concentrations, $dc_{\mathbf{x}}$, was computed as:

$$\text{mld}\, dc_{\mathbf{x}} / dt = F_{as,x} + F_{entr,x} \quad (5)$$

where mld is mixed layer depth. The air-sea flux term, F_{as}, was separated into several components; diffusive gas exchange, F_{dif}, injection of small bubbles, F_{inj}, and air-water interface exchange across larger bubble surfaces, F_{ex}. These gas exchange terms were all scaled to the fraction of open water, A, following Loose et al. (2009), as described in section 2.4. The total air-sea flux term (F_{as}) for gas x was thus computed as:

$$F_{as,x} = (F_{dif,x} + F_{inj,x} + F_{ex,x}\ )\ (1 - A)^{0.4} \quad (6)$$

$$F_{dif,x} = -k_x\ (c_x - \alpha_x\ p_x) \quad (7)$$

$$F_{inj,x} = A_{inj}\ p_x\ (u_{10} - 2.27)^3 \quad (8)$$

$$F_{ex,x} = A_{ex}\ p_x\ (D_x / 1\ m^2\ s^{-1})^{0.5}\ (\alpha_x / 1\ mol\ m^{-3}\ atm^{-1})\ (u_{10} - 2.27)^3 \quad (9)$$

where k_x is the gas transfer velocity (m s^{-1}) calculated following Sweeney et al. [2007], α_x the solubility (mol m^{-3} atm^{-1}), p_x the partial pressure calculated from the mole fraction in dry air and the dry atmospheric pressure ($p_x = \chi_x\, p_{atm,dry}$), and D_x the diffusion coefficient (m^2 s^{-1}). The injection and exchange rates A_{inj} and A_{ex} (mol s^2 m^{-5} atm^{-1}) given in Nicholson et al. [2011] were derived for average wind speeds. For our calculations based on short-term wind-speeds, we use a flux enhancement factor, R, of 1.5 as discussed in Nicholson et al. [2011]. The bubble fluxes F_{inj} and F_{ex} scale with whitecap coverage (0 for $u_{10} < 2.27$).

The entrainment term is governed by the change in mixed layer depth (only deepening of the mixed layer impacts the surface water budget), and by difference between mixed layer concentration c_x and the concentration in the sub-surface layer $c_{x,sub}$:

$$F_{entr} = (c_{x,sub} - c_x)\, d(\text{mld}) / dt \qquad (10)$$

The changes in mixed layer depth used to quantify the physical entrainment term were obtained from temperature and salinity profiles of the Mercator global operational system PSY3V3. These model-derived mixed layer depths, which assimilate all available measurements in a given study region, showed reasonable agreement with values obtained from our actual CTD observations ($r = 0.61$), and were able to reproduce the spatial patterns in mixing depths across our cruise track (Fig. S1). Moreover, comparison of the time-dependent model MLD history, with observations derived from Argo float data showed that the model output was able to reproduce the significant changes in MLD (including a number of pronounced deepening events) observed across our study region (Fig. S2).

For N_2, the choice of the sub-mixed layer concentration $c_{N_2,sub}$ has a minor influence on the calculation given the weak vertical gradients of this gas in the absence of a sub-surface biological production or consumption term. We thus chose a uniform value of 100 % surface saturation for $c_{N_2,sub}$. In the case of O_2, however, strong vertical gradients and variable saturation levels have a significant influence on the entrainment term, and the choice of $c_{O_2,sub}$ values can thus exert a significant influence on the model calculations under conditions of mixed layer deepening. Given our interest in comparing physical and biological processes affecting the surface water O_2 balance, we computed two different O_2 entrainment terms. The first term,

352 ΔO_{2pe}, reflects the entrainment of sub-surface waters in the absence of a biological signature.
353 For this calculations the sub-surface O_2 end-member ($c_{O_2,sub}$) was set to 100 %, as in the N_2
354 calculations. We also computed a total O_2 entrainment term, ΔO_{2te}, which reflects the bulk
355 transport of O_2 into the mixed layer, based on the observed difference in O_2 concentrations
356 between surface and sub-surface waters. For these calculations, we used the average O_2
357 concentration 20 – 25 m below the mixed layer depth to define the end member concentration
358 ($c_{O_2,sub}$) for entrained waters. This depth was chosen based on examination of mixed layer depth
359 history from the PSY3V3 output during a number of modelled entrainment events. The mean
360 $c_{O_2,sub}$ end member values were calculated from CTD data for each sampling station, and
361 interpolated to the full resolution of our cruise track for use in the entrainment calculations.
362 The model mixed layer concentrations of O_2 and N_2 were initialized at 100 % saturation
363 starting 30 d prior to the underway measurements. The ancillary data (*e.g.* wind speed,
364 atmospheric pressure, mixed layer depth *etc.*) were interpolated to the cruise track position and
365 time, and used to force the model calculations for 30 d with time-steps of 6 h.
366
367 **2.7** ***Net community production estimates***
368 We used the approach of Reuer et al. [2007] to estimate net community production (NCP,
369 *i.e.* gross photosynthesis minus community respiration) from our mixed layer ΔO_2 /Ar
370 measurements. The calculations presented by Reuer et al. [2007] are based on a steady-state
371 model, where lateral advection and vertical entrainment are assumed to be negligible, and the
372 mixed layer O_2 mass balance is influenced solely by NCP and gas exchange. Under these
373 conditions, steady-state NCP is equivalent to the air-sea flux of biogenic O_2 (obtained from ΔO_2
374 /Ar and the air-equilibrium O_2 concentration, $\alpha_{O_2} * p_{atm}$). The gas exchange term, k, is derived
375 using a weighting function to account for variability in wind speed history over the residence
376 time of O_2 in the mixed layer (see Reuer et al. [2007] for details).
377
378 $$NCP = \Delta O_2 /Ar * \alpha_{O_2} * p_{atm} * k \quad (11)$$
379

For consistency with our box model calculations, we used the gas exchange parameterization (k) of Sweeney et al. [2007], and the ice-dependent scaling factor of Loose et al. [2009] to derived NCP estimates.

We recognize that the assumptions required for the ΔO_2 /Ar-based NCP calculations are unrealistic for at least some portions of our cruise track where entrainment of sub-surface waters into the mixed layer is likely non-negligible. To examine the influence of mixed layer entrainment on NCP, we used the output from our box model calculations (see above) to estimate the O_2 flux associated with changes in mixed layer depth. Based on our calculation of ΔO_{2pe} and ΔO_{2te}, we derived a specific biological entrainment term, ΔO_{2be}, for use in the correction of ΔO_2 /Ar for NCP calculations.

$$\Delta O_{2be} = \Delta O_{2te} - \Delta O_{2pe} \quad (12)$$

This term reflects the entrainment of biologically-modified O_2 signatures from sub-surface waters. The purely physical entrainment term, ΔO_{2pe}, affects O_2 and Ar in a nearly identical manner, and thus has a negligible influence on the measured ΔO_2 /Ar ratio. In contrast, ΔO_{2be} specifically affects O_2, and thus modifies ΔO_2 /Ar. Our approach, based on the separation of biogenic and non-biogenic entrainment fluxes thus allows us to correct the observed ΔO_2 /Ar values for entrainment of biologically-modified sub-surface waters, after removing the non-biological entrainment signature. We used the corrected ΔO_2 /Ar data as input to equation 11. Given the physical complexity of our study region, and its high degree of temporal variability, we treat our NCP calculations as a first order estimate of biological O_2 production rates in the mixed layer, recognizing the quantitative limitations of this approach.

Additional NCP estimates were derived from an analysis of seasonal mixed layer DIC deficits as described in section 2.5. In order to estimate a mean daily NCP rate from these seasonal deficits, it is necessary to choose an integration time-scale (*i.e.* the length of time over which the DIC deficit has accrued). We obtained an estimate of the integration time-scale using an analysis of 8-day AquaModis Chla imagery provided by Oregon State University, with a cloud filling algorithm (http://www.science.oregonstate.edu/ocean.productivity/). We computed mean Chla concentrations in three geographic regions centered around the N-S, E-W and WAP sections of our cruise track, and used these values to reconstruct the history of surface Chla

411 concentrations in each sub-region (Fig. S3). The approximate initiation date of positive NCP
412 was then derived as the first significant increase in Chl *a* concentrations over winter-time values,
413 and the NCP integration times for DIC deficits were obtained from the difference between the
414 mean sampling date and the calculated bloom initiation date in each of the three regions. We
415 obtained integration times of 69, 50 and 98 days for the N-S, E-W and WAP regions,
416 respectively. We used a photosynthetic quotient of 1.4 mol O_2 : mol DIC [*Laws*, 1991] to
417 convert DIC-based NCP to O_2 units for comparison with our ΔO_2 /Ar-based NCP estimates.
418

419 ## 3. Results and Discussion

420

421 ### *3.1 Surface water hydrography and Chla*

422 Sea surface temperature (SST) exhibited a strong latitudinal gradient along the northern
423 portion of the N-S transect, across the transition from sub-tropical to Antarctic waters (Figures
424 2a, 3d). In contrast, the ice covered waters south of the SBdy frontal zone were characterized by
425 near homogeneous SST (± 0.3˚C) close to the freezing point of seawater. Along the E-W and
426 WAP transects, SST ranged from -1.8 to 3 ˚C, and exhibited significant spatial heterogeneity
427 (Figures 2a, 3d). The relatively warm SST of the WAP region reflects the influence of surface
428 warming in shallow near-shore waters, and/or the signature of modified circumpolar deep water
429 (MCDW) flowing onto the continental shelf [*Martinson and McKee*, 2012]. Salinity also
430 showed significant spatial variability across the E-W and WAP regions. Relatively fresh waters
431 (salinity ~ 33.2), indicative of local sea ice melt, were observed along the Weddell Sea MIZ at ~
432 42˚W and along the WAP in the near shore waters adjacent to Marguerite Bay (Figure 2b).
433 Mixed layer depths, computed from CTD profile data, ranged from < 10 m to ~ 100 m, with an
434 overall mean of 26 m (± 20 m std. dev.). The shallowest mixed layer depths were observed in
435 low salinity regions along the western portion of the Weddell Sea MIZ and in near shore waters
436 of the WAP.
437 Strong gradients in surface hydrography were associated with significant variability in
438 phytoplankton Chla fluorescence. Pelagic waters of the N-S transect were generally
439 characterized by relatively low Chla fluorescence, although elevated values were observed along
440 frontal zones of the SAF, PF, SACCF and SBdy (Fig. 2d, 3c). Increased Chla concentrations
441 along frontal zones are a well known feature of the Southern Ocean that has been attributed to

the supply of nutrients through enhanced vertical mixing [*Laubscher et al.*, 1993; *Sokolov and Rintoul*, 2007; *Sokolov*, 2008]. The intensity of this mixing is particularly strong in the polar frontal region, where we observed the greatest enhancement of surface Chla fluorescence. Relative to the N-S transect, waters of the Weddell Sea MIZ and near shore regions of the WAP showed extreme variability in Chla fluorescence. Values ranged by more than two orders of magnitude, and exhibited sharp gradients over small spatial scales, often in regions of local sea-ice melt (Fig. 3c). Previous studies have demonstrated a strong influence of sea-ice processes on phytoplankton growth in surface waters [*Arrigo and van Dijken*, 2004; *Smith and Nelson*, 1985]. Melting ice can stimulate phytoplankton growth through the release of Fe [*Gerringa et al.*, 2012; *Sedwick and DiTullio*, 1997] and/or decreasing surface salinity, which acts to stabilize the mixed layer. Indeed, we observed a negative relationship between Chla fluorescence and salinity in the WAP (r = -0.42) and, to a lesser extent, along the E-W transit. (r = -0.17). The relationship between biological productivity and mixed layer depth is addressed in section 3.6.

3.2 ΔO_2 /Ar and pCO_2 distributions

Along the N-S transect, ΔO_2 /Ar was generally within a few percent of atmospheric equilibrium, with slightly positive values north of 55˚S (< 2000 km along the cruise track) and negative values in ice-covered waters of the Weddell Sea MIZ (Figure 2f, Figure 3b). Negative ΔO_2 /Ar values are indicative of net heterotrophic conditions under the sea ice and/or the presence of deep mixed layers bearing a remnant heterotrophic signature. Although relatively few pCO_2 data are available for the N-S transect, we observed a sharp pCO_2 gradient (from 450 to 330 µatm) on the southern edge of the MIZ (Figure 2e, 3a). Surface water pCO_2 and ΔO_2 /Ar showed high variability in the Weddell Sea MIZ (E-W transect) and WAP region. In these areas, pCO_2 reached minimum values of ~ 100 µatm, while ΔO_2 /Ar in excess of 50% was observed (Figure 3a,b). The lowest pCO_2 and highest ΔO_2 /Ar occurred in near shore waters of Marguerite Bay (WAP; Figure 2e,f) at ~11,000 km along our cruise track.

The pCO_2 and ΔO_2 /Ar disequilibria we observed are substantially higher than values previously reported for the offshore pelagic Southern Ocean [*Cassar et al.*, 2011; *Reuer et al.*, 2007; *Shadwick et al.*, 2014], but they are consistent with recent observations from the highly productive waters of the Ross Sea and Amundsen Sea polynyas [*Smith and Gordon*, 1997;

Tortell et al., 2011; *Tortell et al.*, 2012]. In sections 3.5 and 3.6, we discuss the relative contributions of physical and biological processes to O_2 supersaturation. Here, we note only that ΔO_2/Ar was positively correlated with Chla (r = 0.66 and 0.43 along the E-W and WAP transects, respectively), and showed enhancements in frontal zones along the N-S transect. Unlike ΔO_2 /Ar, pCO_2 is sensitive to temperature-dependent solubility changes. During the 30 days prior to our sampling, the NOAA OISST data show an average surface water warming of ~ 1 ˚C along our cruise track. This warming would lead to a 4% (~ 15 μatm) increase in pCO_2 [*Takahashi et al.*, 2002], which is small compared to the observed pCO_2 variability along the cruise track. This result indicates that biological uptake exhibited a first order control on pCO_2 distributions.

As expected, pCO_2 exhibited a strong negative correlation with ΔO_2 /Ar along our cruise track (Pearson's correlation coefficient, r = -0.85 and -0.91 for the E-W and WAP regions, respectively). Figure 4 shows the corresponding relationship between O_2 and total dissolved inorganic carbon (DIC) concentrations derived from pCO_2 and ΔO_2 /Ar data. For both the WAP and E-W regions, the slope of the O_2 : DIC relationship was significantly lower than the expected photosynthetic stoichiometry (photosynthetic quotient, PQ, 1.0 - 1.4 mol O_2 : mol DIC; [*Laws*, 1991]). This discrepancy can be explained by the differential rate of sea-air O_2 and CO_2 exchange. Faster air-sea equilibration of O_2 results in a shorter residence time of this gas in the mixed layer, and a more rapid ventilation of photosynthetically-derived O_2. During our cruise, the average residence time of O_2 in the mixed layer was < 1 week, given the mean wind speed (9.2 m s^{-1}) and MLD (26 m) observed across the survey region. In contrast, disequilibria in pCO_2, which is buffered by the seawater carbonate system, can persist for many weeks and even months in the surface mixed layer [*Takahashi et al.*, 2009]. The degree of uncoupling between CO_2 and O_2 in the mixed layer should thus provide insight into temporal evolution of biological productivity in surface waters. Regions where the biological production signal is 'older' should exhibit a higher degree of CO_2 – O_2 uncoupling. In our data set, the lower O_2-DIC slope in the WAP region (0.33 vs. 0.45 for the E-W transect; Fig. 4) suggests that the production signal was integrated over a longer time interval. Indeed, remote sensing data show the presence of phytoplankton blooms in the WAP for over two months prior to our sampling (see Fig. 8b and section 3.6). In contrast, much of the biological production along the E-W region occurred following recent ice retreat, with shorter time interval for gas exchange to uncouple O_2 and DIC.

503 Similar observations on the time-dependent coupling of CO_2 and O_2 coupling have been recently
504 reported by Shadwick et al. [2014] although these authors did not present derived O_2 and DIC
505 concentrations.
506
507 ***3.3 Sea-air CO_2 fluxes***

508 During the time of the survey, our sampling region served as a strong CO_2 sink. Along the
509 E-W transit, CO_2 fluxes showed a bimodal distribution (Fig. 5), with an overall mean of -13.0 ±
510 6.70 (std. dev.) mmol m^{-2} d^{-1}, and a range of -41.4 to -2.76 mmol m^{-2} d^{-1} (negative fluxes signify
511 oceanic uptake). For the WAP region, the mean CO_2 flux was -9.26 ± 5.51 mmol m^{-2} d^{-1} (range -
512 -32.3 to +7.43). In both the WAP and E-W regions, the frequency distribution of CO_2 fluxes
513 (Fig. 5) exhibited a long tail at low values (oceanic uptake). The strongest oceanic CO_2 uptake
514 along the entire cruise track (> 40 mmol m^{-2} d^{-1}) was observed near Marguerite Bay along the
515 WAP, while a small net CO_2 efflux from surface waters was observed north of the WAP in
516 pelagic waters of the Drake Passage.
517 Current estimates of regional air-sea CO_2 fluxes in the Southern Ocean are based on the
518 climatology of Takahashi et al. [2009], compiled from a global compilation of field
519 measurements. This climatology indicates a weak to moderate Southern Ocean CO_2 sink
520 between ~ 40 and 50 ˚S (between the STF and PF), and suggests that waters south of the PF are
521 either neutral or slight sources of CO_2 to the atmosphere. However, actual data coverage is
522 sparse over much of the high latitude Southern Ocean, particularly in the MIZ and the
523 continental shelf regions. Examination of the underlying pCO_2 dataset used to construct the
524 2009 climatology, shows very few summer time (December and January) pCO_2 observations in
525 the Weddell Sea MIZ, with many grid cells lacking primary data, and fluxes derived from
526 interpolation of the nearest available observations. Moreover, the resolution of the climatology
527 grid cells (4˚ x 5˚) is coarse relative to the observed length scales of variability. For these
528 reasons, it is likely that significant features are not well represented in the climatological maps of
529 Southern Ocean CO_2 fluxes.
530 In Fig. 5, we have plotted our cruise track over the gridded CO_2 fluxes of Takahashi et al.
531 [2009]. Our sampling region encompassed ~ 25 grid cells (7 of which lacked primary data), and
532 we derived mean CO_2 fluxes and air-sea CO_2 gradients (ΔCO_2) for these areas. The results,
533 shown in Table 1, highlight a significant difference between the CO_2 fluxes derived from our

MIMS data, and those from the climatology. In December, the climatology shows our sampling region to be near neutral with respect to air-sea CO_2 fluxes (1.4 ± 0.90 mmol m^{-2} d^{-1}), whereas our measurements show mean oceanic uptake of 10 (± 5.8) mmol m^{-2} d^{-1}. In January, the climatological CO_2 flux is -2.4 ± 0.92 mmol m^{-2} d^{-1}, compared to -9.9 ± 4.2 mmol m^{-2} d^{-1} derived from our measurements. The climatology represents a mean value derived from many years of observations, and some inter-annual variability is expected. During our survey, we measured significantly higher air-sea CO_2 disequilibria than are present in the climatology; for December and January, respectively, we observed an average ΔCO_2 of -91 and -108 μatm, compared to the climatological values of ~ +17 and -39 μatm. These differences are likely too large to represent simple inter-annual variability, and likely reflect real differences in the underlying distribution of data. Our results thus suggest significantly higher oceanic CO_2 uptake in high latitude Antarctic waters than is represented by the global climatology. Similar observations have been reported in previous studies [*Arrigo et al.*, 2008; *Bellerby et al.*, 2004; *Hoppema et al.*, 2000a]. Note that the apparent difference in sea-air CO_2 fluxes between our observations and the climatology is ~ 2-fold larger if we compute the fluxes using ship-based winds as opposed to the weekly averaged NCEP reanalysis product.

High latitude Antarctic waters, and the MIZ in particular, should be effective at sequestering CO_2 from the atmosphere due to the coupling of biological productivity with sea ice dynamics. As observed in our study and that of previous authors [*Bakker et al.*, 2008; *Jones et al.*, 2010], ice retreat leads to enhanced phytoplankton biomass and strong CO_2 uptake. Previous studies have shown that much of the CO_2 taken up by spring phytoplankton growth can effectively be sequestered into sub-surface layers during late summer cooling and the return of ice cover at the end of the growing season [*Sweeney*, 2003]. Late season sea ice cover acts to limit outgassing of high CO_2 during the net heterotrophic period of the annual growing season, enhancing the CO_2 sequestration efficiency of surface waters. For this reason, Antarctic continental shelf waters are likely to contribute disproportionately to Southern Ocean CO_2 uptake [*Arrigo et al.*, 2008]. Inclusion of more data from these regions into updated climatologies (with finer-scale grid cell resolution, and greater seasonal data coverage) could lead to revised estimates of Southern Ocean CO_2 uptake, with significant implications for the global C budget.

3.4 ΔN_2 *distribution*

565 Across much of our sampling region, N_2 was supersaturated with respect to atmospheric
566 equilibrium (*i.e.* $\Delta N_2 > 0$; Fig. 2c, 6a). The one exception occurred in an ice-covered region of
567 the Weddell Sea (~6,500 km), where we measured a ΔN_2 of ~ -1 %. This feature may reflect the
568 low atmospheric pressure ~ 7 days prior to our arrival on station, or the recent release of cold and
569 fresh melt water that is undersaturated in N_2 (due to gas exclusion from the forming ice matrix).
570 The average ΔN_2 along the full cruise track was ~ +2.5 %, with maximum values of ~ +6 %
571 observed in regions of high wind speed (> 20 m s^{-1}) and/or decreasing atmospheric pressure
572 along the northern portion of the N-S transect (in the SACCF region), the Weddell Sea
573 continental margin and the northern WAP (Figure 6). In some cases (e.g. ~11,000 km cruise
574 track distance), strong N_2 supersaturation was associated with recent warming of the mixed layer,
575 and decreased gas solubility. The maximum ΔN_2 values we observed are significantly higher
576 than those reported previously for mid-latitude oceanic regions [*Emerson et al.*, 2008; *McNeil et*
577 *al.*, 2005; *Vagle et al.*, 2010], including recent observations from the Sub-Antarctic zone of the
578 Southern Ocean [*Weeding and Trull*, 2014], where ΔN_2 did not exceed ~ +3 % during an
579 observation period of 7 months. Our observations may be indicative of a persistently high ΔN_2
580 signal across large areas of the S. Ocean, driven by high regional wind speeds and strong
581 changes in atmospheric pressure.
582 Box model calculations of ΔN_2, based on gas exchange processes and mixed layer
583 entrainment [*Nicholson et al.*, 2011], were used to examine the various processes contributing to
584 the high ΔN_2 across our survey region. In general, the calculated ΔN_2 values were in good
585 agreement with our observations, and the model was able to reproduce both the absolute
586 magnitude of ΔN_2 and its spatial variability along much of our cruise track (Figure 6a). In a
587 number of instances, however, modelled ΔN_2 was significantly lower than the observed values,
588 particularly at the beginning and end of the HGTD data record. While it is possible that offsets
589 between observations and model output at the end of the data reflect problems with the HGTD
590 before its failure, several sources of uncertainty are also present in our calculations. The 1D
591 model we used for our calculations does not account for advection of water masses with possibly
592 different pre-formed gas concentrations. The dynamic system of frontal zones between Cape
593 Town and the Polar Front may thus explain part of the discrepancy between observations and
594 model output during the northern portion of the N-S transect. The remainder of our survey region

595 is less prone to advection, owing to a (zonally) more homogeneous water mass structure. In the
596 MIZ, uncertainty in the model calculations may result from sea-ice dependent processes. The
597 sea ice history used in the model was derived from reprocessed satellite data with a relatively
598 coarse spatial resolution. Sea ice cover exerts a significant influence on the strength of air-sea
599 exchange, and errors in the representation of sea ice cover or in the parameterization of ice
600 effects on gas exchange coefficients [*Loose et al.*, 2009] would lead to uncertainty in the ΔN_2
601 calculation. Notwithstanding these sources of uncertainty, we conclude that our observations
602 provide a reasonable validation of the Nicholson et al. [2011] model in various Southern Ocean
603 regions with high wind speeds and strong temporal changes in atmospheric pressure. Additional
604 GTD data and higher resolution physical models will be needed to further examine the
605 distribution of ΔN_2 across various Southern Ocean regions. Inclusion of GTD sensors on new
606 biogeochemical ocean floats and gliders [*Emerson et al.*, 2002; *Nicholson et al.*, 2008] will be
607 particularly useful in this respect.
608
609 ***3.5 Physical vs. biological controls on O_2 saturation states***

610 Unlike N_2, oxygen saturation states are strongly influenced by both physical and biological
611 processes. We quantified the physical effects on O_2 saturation state (ΔO_{2phys}), using
612 simultaneous MIMS and optode measurements (see methods). Measured values of ΔO_{2phys} (*i.e.*
613 optode ΔO_2 – MIMS ΔO_2 /Ar) showed significant variability along our cruise track (Fig. 7a),
614 with values ranging from ~ -5% (undersaturation) to > +10% (supersaturation). This range of
615 values is significantly larger than that reported recently by Shadwick et al. [2014], who measured
616 ± 3% ΔO_{2phys} along a transect from Australia to the Antarctic MIZ. In our study, maximum O_2
617 supersaturation was observed in the WAP region (~ 11,000 km cruise track), whereas
618 undersaturation was largely confined to several regions of local sea-ice cover (Fig. 7a). Box
619 model calculations of ΔO_{2pe} (*i.e.* the entrainment of non-biologically modified sub-surface
620 waters) showed reasonably good agreement with observations, and were able to reproduce the
621 spatial pattern of ΔO_{2phys} along much of the cruise track (Fig. 7a). There were, however, notable
622 offsets between the modelled and observed values in some areas, with the model tending to
623 under-predict the observations, as seen for ΔN_2 (Fig. 6). The largest discrepancies between the
624 model and observations occurred along the N-S transect, and in the WAP region. As discussed

above for ΔN_2, the discrepancy between modelled and observed ΔO_2 along the N-S transect may have resulted from the lateral advection of heterogeneous waters masses. By comparison, the high apparent values of ΔO_{2phys} measured in the WAP (in excess of +10%) are more difficult to reconcile with known physical processes driving O_2 supersaturation in the mixed layer. Given the extremely high O_2 concentrations in this region (> 60% O_2 supersaturation), the optode was measuring at the outer limit of its calibration range, and we cannot exclude measurement errors leading to an overestimation of ΔO_{2phys}. Moreover, the shallow mixed layers and bottom depths in the coastal WAP make this region susceptible to physically induced O_2 super-saturation resulting from bubble injection under high wind speeds. Under these conditions, our calculations, which assume 100% O_2 saturation in sub-surface waters, would underestimate ΔO_{2pe}.

In addition to our calculations of ΔO_{2pe}, we used the box model to derive an O_2 entrainment term associated with the transport of biologically-modified waters into the mixed layer. This entrainment term, ΔO_{2be}, can be used to correct ΔO_2/Ar-derived NCP estimates, neglecting the contribution of purely physical entrainment processes (ΔO_{2pe}) that have no significant effect on ΔO_2 /Ar. The distribution of modelled ΔO_{2be} along the cruise track is shown in Fig. 7b, along with our ΔO_2 /Ar observations. For much of our survey region, the magnitude of the biologically-modified entrainment flux was small compared to the mixed layer ΔO_2 /Ar signal. There were, however, a number of areas (particularly along the N-S transect), where the two O_2 fluxes were similar in magnitude. The variability in modelled ΔO_{2be} results from differences in O_2 depth profiles and mixed layer depth history along the cruise track. Under conditions where sub-surface O_2 is lower than mixed layer values, due to net heterotrophy in the sub-euphotic zone, entrainment of biologically-modified sub-surface waters acts to decrease the O_2 saturation in the mixed layer (*i.e.* $\Delta O_{2be} < 0$). This phenomenon was clearly observed in the ice-covered waters of the N-S and E-W transects (Fig. 7b) where ΔO_{2be} showed a clear negative signature. In contrast, we observed a number of regions, mostly in the WAP, where ΔO_{2be} was positive, reflecting the entrainment of a remnant productivity signal prior to mixed layer shoaling. Jonsson et al. [2013] have also noted the importance of entrainment as a potential source of O_2 into the mixed layer. Quantification of this O_2 source depends on an understanding of mixed layer depth history and the choice of an appropriate sub-surface O_2 end-member ($c_{O_2,sub}$). Based

655 on an analysis of the mixed layer time-series produced by the PSY3V3 model output, we chose a
656 subsurface O_2 end-member ($c_{O_2,sub}$) 20 - 25 m below the mixed layer. We note, however, that
657 these end-member O_2 values, and the corresponding mixed layer histories are subject to
658 potentially significant uncertainty. Nonetheless, as discussed below, we found that the derived
659 ΔO_{2be} term was able to produce entrainment-corrected ΔO_2 /Ar-NCP values that showed good
660 agreement with independent estimates based on DIC deficit calculations. It is also important to
661 note that the entrainment term was generally small compared to the biological O_2 production
662 signal (*i.e.* ΔO_2/Ar) in the mixed layer for much of our survey region.
663
664 ***3.6 Net Community Production***

665 In recent years, a number of studies have examined Southern Ocean NCP using mixed layer
666 ΔO_2 /Ar measurements, both from discrete samples and continuous underway analysis. This
667 work has been largely based on the approach developed by Kaiser et al. [2005] and Reuer et al.
668 [2007], where the mixed layer O_2 budget is assumed to be in a steady-state, with negligible
669 vertical or lateral fluxes. Under these conditions, the biologically-induced flux of O_2 to the
670 atmosphere (O_2-bioflux, as defined by Eq. 11) provides a measure of NCP. The assumptions
671 used in these calculations are problematic in weakly stratified and highly dynamic waters
672 encountered over large portions of the Southern Ocean. Jonsson et al. [2013] have shown that
673 O_2-bioflux provides good regional estimates of Southern Ocean NCP (± ~ 25%), but significant
674 offsets can exist at smaller scales due to a temporal decoupling between O_2 production and air-
675 sea exchange, and to vertical O_2 fluxes across the base of the mixed layer. Using our box model
676 results (section 3.5), we were able to estimate the contribution of entrainment fluxes to the
677 surface biological O_2 budget, and we used this information to correct NCP estimates derived
678 from surface ΔO_2/Ar data. However, our calculations do not include other physical processes
679 such as upwelling and diapycnal mixing that can also influence NCP derived from ΔO_2/Ar
680 measurements [*Jonsson et al.*, 2013].

681 Figure 8 presents NCP estimates along our cruise track derived from ΔO_2/Ar, with and
682 without a correction for biologically-modified entrainment fluxes (ΔO_{2be}). The figure also shows
683 satellite-derived Chla observations, which provide information on the temporal evolution of
684 phytoplankton biomass prior to our sampling. Across the full survey region, O_2 /Ar-derived

685 NCP ranged from ~ -40 to > 300 mmol O_2 m^{-2} d^{-1}. The lowest NCP values were found along the
686 N-S transect (maximum ~ 20 mmol O_2 m^{-2} d^{-1}). Despite the low overall productivity observed
687 along much of this transect, there were localized regions of elevated NCP associated with
688 regional frontal features - most notably in the vicinity of the Polar Front zone where vertical
689 mixing can supply Fe to iron-limited surface waters [*Debaar et al.*, 1995]. Without a correction
690 for entrainment, waters of the Weddell Sea MIZ (both along the N-S and E-W transects)
691 appeared to be net heterotrophic (*i.e.* NCP <0). However, this apparent net heterotrophic
692 signature was eliminated after accounting for the entrainment fluxes (ΔO_{2be}). In contrast, the
693 entrainment-corrected NCP remained below zero in the STF zone, and in several other localized
694 regions along the cruise track. Net heterotrophy in the STF zone seems unlikely, given the
695 enhanced Chla concentrations in this region (Fig. 3c). Rather, we suggest that an overestimation
696 of the O_2 entrainment term (ΔO_{2be}), resulting from errors in the selection of a sub-MLD end-
697 member or in the derived mixed layer depth history, is a more likely explanation for this feature.
698 Regions of net heterotrophy observed along other portions of our cruise track (*e.g.* between 8000
699 - 9000 km) were largely confined to waters with very low (< 0.3 μg L^{-1}) Chla concentrations. In
700 contrast, the most productive waters, with NCP in excess of 300 mmol O_2 m^{-2} d^{-1} were observed
701 in the central WAP region, where high phytoplankton biomass was detected for over two months
702 prior to our sampling. In these high NCP waters, the entrainment correction term was generally
703 small compared to the biological production term.

704 The variability of our ΔO_2/Ar-derived NCP values is somewhat higher than previous
705 observations for the Southern Ocean, but the mean values for each of survey regions are within
706 the range of recently published estimates. Excluding the negative NCP values in the STF zone,
707 the average NCP for the N-S, E-W and WAP transects was 9.3, 31 and 14 mmol O_2 m^{-2} d^{-1},
708 respectively. The low mean NCP value for the WAP region seems initially surprising, given the
709 extremely elevated NCP observed at ~ 11,000 km along the cruise track. Outside of this one
710 productivity hot-spot, however, much of the WAP region had relatively low (and in some cases
711 even negative) NCP. Excluding the negative values, the mean NCP value in the WAP is 48
712 mmol O_2 m^{-2} d^{-1}. By comparison, exclusion of negative NCP values from the E-W transect only
713 increased the mean NCP by ~ 10%. These results suggest that localized net heterotrophy was
714 more significant to regional NCP budgets in the WAP region.

715 Based on discrete sampling of surface $\Delta O_2/Ar$, Reuer et al. [2007] reported mean NCP
716 estimates ranging from 20 – 36 mmol O_2 m^{-2} d^{-1} for the Subantarctic Zone, Polar Frontal Zone
717 and Antarctic Zone. More recently, Shadwick et al. [2014] have reported a range of NCP
718 estimates from 15 – 75 mmol O_2 m^{-2} d^{-1} (assuming a photosynthetic quotient of 1.4) along a
719 transect from Australia to the Antarctic continent, while Cassar et al. [2011] report NCP of ~ up
720 to 150 mmol O_2 m^{-2} d^{-1} for sub-Antarctic waters south of Australia. The maximum NCP values
721 measured along our cruise track (> 300 mmol O_2 m^{-2} d^{-1}) are among the highest reported for the
722 Southern Ocean, yet these values are not without precedent. Recent time-series work at the
723 Palmer Station LTER site along the WAP [*Tortell et al.*, 2014], show maximum NCP values
724 similar to the highest values we observed along the WAP region of our cruise track.
725 Independent NCP estimates, based on calculated seasonal DIC deficits at discrete sampling
726 stations, showed good general coherence with our ΔO_2 /Ar-derived values. Both the spatial
727 distribution and range of NCP values were similar for the two methods. The agreement between
728 the two estimates was particularly good in the WAP region (unfortunately, DIC samples were
729 not collected in the vicinity of Marguerite Bay, where the highest NCP values were observed),
730 and also south of the SBdy frontal zone along the N-S transect. In contrast, there were apparent
731 offsets between the two NCP estimates in the vicinity of the PF and in the highest productivity
732 regions of the E-W transit. In addition to the uncertainties discussed above for ΔO_2 /Ar-derived
733 NCP, NCP estimates from DIC deficits are also subject to potential errors. The most significant
734 source of uncertainty in these calculations relates to the time-period over which DIC uptake is
735 normalized. In our analysis, we assumed that DIC deficits began to accumulate following the
736 initiation of the spring phytoplankton blooms (as judged by satellite-based chlorophyll
737 measurements; Fig. S3). This approach does not account for potential productivity under sea-ice
738 [*Arrigo et al.*, 2012], which is not visible by remote sensing. Although our approach is, by
739 necessity, somewhat simplistic, we are encouraged by the good correspondence of DIC and
740 $\Delta O_2/Ar$-derived estimates of surface water productivity. Our results suggest that mixed layer
741 ΔO_2 /Ar measurements have the capacity to provide meaningful NCP estimates with high spatial
742 resolution.
743 Beyond the absolute value of our derived NCP estimates, the spatial distribution of
744 biological productivity across our survey region is of interest. Since macro-nutrients were
745 plentiful across our entire survey region (minimum NO_3^- > 8 μM), light and/or iron availability

746 are the most likely bottom-up controls on phytoplankton productivity. Although no iron data are
747 available for our cruise, we assume, based on previous studies, that Fe availability was highest in
748 regions of sea ice melt along the continental shelf [*Gerringa et al.*, 2012; *Klunder et al.*, 2011],
749 where high NCP was observed. To examine the influence of light availability on surface water
750 productivity, we derived NCP estimates for the regions surrounding each of our hydrographic
751 stations (within 5 km), and correlated these values to the mixed layer depths obtained from CTD
752 data. As shown in Fig. 9, we observed a weak negative trend between NCP and MLD,
753 particularly for stations with mixed layer depths less than 40 m. Taking only stations with MLD
754 < 40 m, the correlation between MLD and NCP was statistically significant (for 1 m binned data,
755 $r = -0.86$, $p < .001$). This relationship provides some evidence for light-dependent productivity,
756 as suggested previously [*Cassar et al.*, 2011; *Huang et al.*, 2012; *Shadwick et al.*, 2014]). We
757 note, however, that instantaneous MLD estimates do not necessarily provide a good indication of
758 light availability over time scales relevant to our NCP calculations. A more refined analysis
759 could be used, taking into account the time-dependent history of MLD, surface irradiance and
760 water column light extinction (based on Chla concentrations). Even without this added
761 complexity, our derived NCP estimates likely reflect the dominant influence of light, nutrient
762 supply and sea ice cover on biological productivity across strongly distinct regions of the
763 Southern Ocean.
764

765 ## 4. Conclusions and Future Directions

766

767 Our results provide new information on the distribution of pCO_2, O_2, and N_2 in contrasting
768 Southern Ocean regions, and insight into the underlying factors driving these distributions.
769 Across our survey region, strong hydrographic variability led to large gradients in phytoplankton
770 biomass, which, in turn, exerted a significant influence on surface water pCO_2 and $\Delta O_2/Ar$
771 distributions. This biological signature was modified by physical processes including sea-air
772 exchange, and mixed layer entrainment. Using our observations and box model calculations, we
773 were able to quantify the physical contributions to surface water O_2 and N_2 disequilibria, and we
774 used this information to refine our estimates of NCP from surface $\Delta O_2/Ar$ observations. The
775 NCP rates derived in this manner were consistent with independent measurements based on
776 surface DIC deficits, providing a high spatial resolution description of biological productivity

777 across the cruise track. Our surface water pCO_2 observations suggest that the high latitude
778 Southern Ocean may be a stronger sink for atmospheric CO_2 than is currently represented in the
779 global climatology [*Takahashi et al.*, 2009]. To the extent that our results are applicable on a
780 broad regional scale, there may thus be a need to critically re-evaluate current estimates of
781 Southern Ocean CO_2 uptake.
782 The increasing availability of autonomous ship-board instruments for surface gas measurements
783 (e.g. optodes, GTDs and sea-going mass spectrometers) has significantly expanded the spatial
784 and temporal coverage of oceanic dissolved gas observations. In the future, continued
785 deployments of these autonomous instruments, along with instrumented floats, gliders and
786 moorings [*Emerson et al.*, 2008; *Nicholson et al.*, 2008], will allow us to assemble a more robust
787 database of Southern Ocean ΔN_2, ΔO_2, ΔO_2 /Ar to help constrain NCP and air-sea exchange
788 processes. Moreover, additional pCO_2 measurements in poorly sampled regions will help to
789 refine mean climatological CO_2 fluxes for the Southern Ocean. In conjunction with increased
790 data coverage, more sophisticated modelling approaches could be used to interpret surface gas
791 distributions, taking into account smaller-scale physical processes that act to perturb the mixed
792 layer mass balance. Improved datasets and models will facilitate more robust NCP and CO_2 flux
793 estimates, and increase our understanding of the Southern Ocean's role in global biogeochemical
794 cycles.
795

5. Acknowledgements

Data are freely available upon request from the corresponding author (ptortell@eos.ubc.ca). Support for this work was provided from the Natural Sciences and Engineering Council of Canada (P. Tortell), the Von Humboldt Foundation (P. Tortell), the UBC Peter Wall Institute for Advanced Studies (P. Tortell), the OCEANET project of the WGL Leibniz Association (A. Körtzinger), the German Science Foundation's O_2-Floats project (grant KO 1717/3-1; H. Bittig), and from the EU project CARBOCHANGE (grant no. 264879; M. Hoppema). We acknowledge the tremendous leadership of the late Eberhard Fahrbach (AWI) as chief scientist for our cruise, and the efforts of Gerd Rohardt (AWI) in the compilation and quality control of all hydrographic data. Christopher Payne and Constance Couture (UBC) provided ship-board technical assistance with the mass spectrometer.

Table 1. Comparison of sea-air CO_2 fluxes ± std. dev. from the MIMS data (E-W and WAP transects) and the monthly climatology of Takahashi et al. [2009]. Average fluxes from MIMS data were derived from values binned into 4˚ x 5˚ boxes to match the resolution of the climatology. Averages reported for the climatology were obtained from grid cells containing MIMS data.

	MIMS Data		Climatology	
	CO_2 Flux (mmol m^{-2} d^{-1})	ΔpCO_2 (μatm)	CO_2 Flux (mmol m^{-2} d^{-1})	ΔpCO_2 (μatm)
December	-10 ± 5.8	-91 ± 59	1.4 ± 0.90	17 ± 11
January	-9.9 ± 4.2	-108 ± 24	-2.4 ± 0.92	-39 ± 14

Figure Legends

Figure 1. Map of the sampling area showing the cruise track (solid red line) and the position of various hydrographic fronts (dotted lines). From north to south, the fronts are: Subtropical Front (STF), Sub-Antarctic Front (SAF), Polar Front (PF), Southern Antarctic Circumpolar Current Front (SACCF) and Southern Boundary of the Antarctic Circumpolar Current (SBdy). The location of mean frontal positions was derived from Orsi et al. [1995]. N-S, E-W and WAP denote different portions of our sampling region, as described in the text. Grey / black shading around the Antarctic continent represents the mean sea ice cover during the period of our survey, derived from the AMSR-E satellite product.

Figure 2. Spatial distribution of sea-surface temperature, SST (a), salinity (b), N_2 saturation, ΔN_2 (c), Chla fluorescence (d), pCO_2 (e), and biological O_2 saturation, ΔO_2 /Ar (f) along the cruise track. Inset figures show a detailed view of the property distributions along the WAP transect. Note that pCO_2 and ΔN_2 data are not available for the full cruise track due to instrument problems.

Figure 3. Distribution of pCO_2 (a), biological O_2 saturation, ΔO_2 /Ar (b), Chla fluorescence (c) and sea surface temperature (d) along the cruise track. Black vertical lines show the demarcation between the different portions of the cruise track, vertical grey shaded bars show regions with more than 50% ice cover and blue shaded areas with dotted lines show the position of different frontal regions.

Figure 4. Relationship between dissolved inorganic carbon (DIC) concentrations and biogenic O_2. DIC values were obtained from MIMS pCO_2 data, using empirically-derived alkalinity values (based on surface salinity). Biogenic O_2 (*i.e.* the amount of excess O_2 in the mixed layer derived from biological production) was computed from ΔO_2/Ar data using a temperature and salinity-dependent O_2 solubility function. Solid lines show the DIC-O_2 relationship for the E-W and WAP portions of the ship track derived from a Type II regression analysis, while dashed lines show the expected DIC-O_2 relationship for a photosynthetic quotient

(PQ) of 1 or 1.4 mol O_2 produced per mol DIC consumed. The slope of the O_2-DIC relationship is 0.45 and 0.33 for the E-W and WAP regions, respectively.

Figure 5. Frequency distribution of air-sea CO_2 fluxes along the E-W and WAP regions of the cruise track (a). Panels (b) and (c) show the ship-track plotted over the monthly climatological CO_2 flux derived from the global climatology of Takahashi et al. [2009]. Negative fluxes imply oceanic uptake of CO_2.

Figure 6. Nitrogen saturation, ΔN_2 (a), atmospheric pressure history (b) and wind speed history (c) along the cruise track. The black line in panel (a) shows the ΔN_2 value derived from GTD measurements, while the red line shows the results of box model calculations (see text for a full description). Grey vertical patches in panel (a) show regions with greater than 50% ice cover. Atmospheric pressure and wind speed data shown in panels (b) and (c) were derived from NCEP re-analysis. The y axis in panels (b) and (c) represents the number of days prior to the ship's arrival at a location along the cruise track.

Figure 7. Effects of physical and biological processes on mixed layer O_2 saturation state. The black line in panel (a) shows observed values of ΔO_{2phys}, derived from MIMS ΔO_2/Ar and optode ΔO_2, while the red line shows the results of box model calculations, including physical terms in the O_2 budget (*i.e.* air-sea processes and entrainment of non-biologically modified sub-surface waters, ΔO_{2pe}). Panel (b) shows biological effects on the surface O_2 budget resulting from in situ NCP (as reflected by surface ΔO_2/Ar measurements) and modelled entrainment of biologically-modified sub-surface waters (ΔO_{2be}). Panel (c) shows O_2 depth profiles along the cruise track derived from CTD observations. The thin black line and crosses represent the computed mixed layer depth, while the thicker line represents a 5 point running mean.

Figure 8. Distribution of net community production (NCP) along the cruise track (a), and the time-history of Chla concentrations derived from the Aqua-Modis remote sensing product (b). Black and grey lines in (a) represent NCP estimates derived from ΔO_2/Ar data, with and without a correction for biologically-modified O_2 entrainment fluxes (ΔO_{2be}). The red crosses in (a) represent NCP estimated from seasonal DIC deficits in the mixed layer. Vertical blue patches

877 in (a) show frontal regions. The black line in (b) shows the location of the research vessel, while
878 white patches denote sea-ice cover. Note the logarithmic scaling of the Chla axis.
879
880 **Figure 9.** Relationship between ΔO_2 /Ar-derived NCP (corrected for biological entrainment
881 fluxes) and mixed layer depth along the cruise track. Full data represent all of the individual
882 NCP estimates derived at CTD stations, while binned data represent average NCP values for
883 each 1 m MLD bin (MLD > 5 m). The solid line represents the best-fit regression between
884 binned NCP and MLD (r = -0.86)
885

References

Arrigo, K. R., and G. L. van Dijken (2003), Phytoplankton dynamics within 37 Antarctic coastal polynya systems, *Journal of Geophysical Research-Oceans*, *108*(C8).

Arrigo, K. R., and G. L. van Dijken (2004), Annual changes in sea-ice, chlorophyll a, and primary production in the Ross Sea, Antarctica, *Deep-Sea Research Part II*, *51*(1-3), 117-138.

Arrigo, K. R., G. van Dijken, and M. Long (2008), Coastal Southern Ocean: A strong anthropogenic CO_2 sink, *Geophysical Research Letters*, 35(21). doi L21602 10.1029/2008gl035624

Arrigo, K. R., D. K. Perovich, R. S. Pickart, Z. W. Brown, G. L. van Dijken, K. E. Lowry, M. M. Mills, M. A. Palmer, W. M. Balch, and F. Bahr (2012), Massive phytoplankton blooms under Arctic sea ice, *Science*, *336*(6087), 1408-1408.

Bakker, D. C. E., M. Hoppema, M. Schroder, W. Geibert, and H. J. W. De Baar (2008), A rapid transition from ice covered CO_2-rich waters to a biologically mediated CO_2 sink in the eastern Weddell Gyre, *Biogeosciences*, 5(5), 1373-1386.

Bellerby, R. G. J., M. Hoppema, E. Fahrbach, H. J. W. de Baar, and M. H. C. Stoll (2004), Interannual controls on Weddell Sea surface water fCO_2 during the autumn-winter transition phase, *Deep Sea Research Part I: Oceanographic Research Papers*, 51(6), 793-808.

Boyd, P. W. (2002), Environmental factors controlling phytoplankton processes in the Southern Ocean, *Journal of Phycology*, *38*(5), 844-861.

Brewer, P. G., A. L. Bradshaw, and R. T. Williams (1986), Measurements of total carbon dioxide and alkalinity in the North Atlantic Ocean in 1981, in The Changing Carbon Cycle, edited, pp. 348-370, Springer.

Caldeira, K., and P. B. Duffy (2000), The role of the Southern Ocean in uptake and storage of anthropogenic carbon dioxide, *Science*, *287*(5453), 620-622.

Carrillo, C. J., R. C. Smith, and D. M. Karl (2004), Processes regulating oxygen and carbon dioxide in surface waters west of the Antarctic Peninsula, *Marine Chemistry*, 84(3-4), 161-179.

Cassar, N., M. L. Bender, B. A. Barnett, S. Fan, W. J. Moxim, H. Levy, and B. Tilbrook (2007), The Southern Ocean biological response to Aeolian iron deposition, *Science*, 317(5841), 1067-1070.

Cassar, N., P. J. DiFiore, B. A. Barnett, M. L. Bender, A. R. Bowie, B. Tilbrook, K. Petrou, K. J. Westwood, S. W. Wright, and D. Lefevre (2011), The influence of iron and light on net community production in the Subantarctic and Polar Frontal Zones, *Biogeosciences*, 8(2), 227-237.

Castro-Morales, K., N. Cassar, D. R. Shoosmith, and J. Kaiser (2013), Biological production in the Bellingshausen Sea from oxygen-to-argon ratios and oxygen triple isotopes, *Biogeosciences*, 10(4), 2273-2291.

Coale, K. H., R. M. Gordon, and X. J. Wang (2005), The distribution and behavior of dissolved and particulate iron and zinc in the Ross Sea and Antarctic circumpolar current along 170 degrees W, *Deep-Sea Research Part I-Oceanographic Research Papers*, 52(2), 295-318.

Craig, H., and T. Hayward (1987), Oxygen supersaturation in the ocean - biological versus physical contributions, *Science*, *235*(4785), 199-202.

Debaar, H. J. W., J. T. M. Dejong, D. C. E. Bakker, B. M. Loscher, C. Veth, U. Bathmann, and V. Smetacek (1995), Importance of iron for phytoplankton blooms and carbon dioxide drawdown in the Southern Ocean, *Nature*, 373(6513), 412-415.

Dickson, A. G., and F. J. Millero (1987), A comparison of the equilibrium constants for the dissociation of carbonic acid in seawater media, *Deep-Sea Research Part a-Oceanographic Research Papers*, *34*(10), 1733-1743.

Dickson, A. G. (1994), Determination of dissolved oxygen in sea water by Winkler titration, *WHP Operations and Methods*, 1-14.

Dickson, A. G., C. L. Sabine, and J. R. Christian (2007), Guide to best practices for ocean CO_2 measurements.

Emerson, S., C. Stump, B. Johnson, and D. M. Karl (2002), In situ determination of oxygen and nitrogen dynamics in the upper ocean, *Deep Sea Research Part I: Oceanographic Research Papers*, *49*(5), 941-952.

Emerson, S., C. Stump, and D. Nicholson (2008), Net biological oxygen production in the ocean: Remote in situ measurements of O2 and N2 in surface waters, *Global Biogeochemical Cycles*, *22*(3).

948 Garcia, H. E., and L. I. Gordon (1992), Oyxygen solubility in seawater - better fitting equations,
949 *Limnology and Oceanography*, *37*(6), 1307-1312.
950 Gerringa, L. J. A., A. C. Alderkamp, P. Laan, C. E. Thuroczy, H. J. W. De Baar, M. M. Mills, G.
951 L. van Dijken, H. van Haren, and K. R. Arrigo (2012), Iron from melting glaciers fuels the
952 phytoplankton blooms in Amundsen Sea (Southern Ocean): Iron biogeochemistry, *Deep*
953 *Sea Research Part II: Topical Studies in Oceanography*.
954 Hamme, R. C., and S. R. Emerson (2004), The solubility of neon, nitrogen and argon in distilled
955 water and seawater, *Deep-Sea Research Part I*, *51*(11), 1517-1528.
956 Hamme, R. C., and S. R. Emerson (2006), Constraining bubble dynamics and mixing with
957 dissolved gases: Implications for productivity measurements by oxygen mass balance,
958 *Journal of Marine Research*, *64*(1), 73-95.
959 Honjo, S., S. J. Manganini, R. A. Krishfield, and R. Francois (2008), Particulate organic carbon
960 fluxes to the ocean interior and factors controlling the biological pump: A synthesis of
961 global sediment trap programs since 1983, *Progress in Oceanography*, *76*(3), 217-285.
962 Hoppema, M., L. Goeyens, and E. Fahrbach (2000a), Intense nutrient removal in the remote area
963 off Larsen Ice Shelf (Weddell Sea), *Polar Biology*, *23*(2), 85-94.
964 Hoppema, M., M. H. C. Stoll, and H. J. W. de Baar (2000b), CO_2 in the Weddell Gyre and
965 Antarctic Circumpolar Current: austral autumn and early winter, *Marine Chemistry*, *72*(2),
966 203-220.
967 Hoppema, M., R. Middag, H. J. W. de Baar, E. Fahrbach, E. M. van Weerlee, and H. Thomas
968 (2007), Whole season net community production in the Weddell Sea, *Polar Biology*, *31*(1),
969 101-111.
970 Huang, K., H. Ducklow, M. Vernet, N. Cassar, and M. L. Bender (2012), Export production and
971 its regulating factors in the West Antarctica Peninsula region of the Southern Ocean,
972 *Global Biogeochemical Cycles*, *26*, 13.
973 Jennings, J. C., L. I. Gordon, and D. M. Nelson (1984), Nutrient depletion indicates high primary
974 productivity in the Weddell Sea.
975 Johnson, K. M., J. M. Sieburth, P. J. L. Williams, and L. Brandstrom (1987), Coulometric Total
976 Carbon-Dioxide Analysis for Marine Studies - Automation and Calibration, *Marine*
977 *Chemistry*, *21*(2), 117-133.

978 Jones, E. M., D. C. E. Bakker, H. J. Venables, M. J. Whitehouse, R. E. Korb, and A. J. Watson
979 (2010), Rapid changes in surface water carbonate chemistry during Antarctic sea ice melt,
980 *Tellus B*.
981 Jonsson, B. F., S. C. Doney, J. Dunne, and M. Bender (2013), Evaluation of the Southern Ocean
982 O2/Arâ€ based NCP estimates in a model framework, *Journal of Geophysical Research:*
983 *Biogeosciences*, *118*(2), 385-399.
984 Kaiser, J., M. K. Reuer, B. Barnett, and M. L. Bender (2005), Marine productivity estimates
985 from continuous O_2/Ar ratio measurements by membrane inlet mass spectrometry,
986 *Geophysical Research Letters*, *32*(19).
987 Keeling, R. F. (1993), On the role of large bubbles in air-sea gas exchange and supersaturation in
988 the ocean, *Journal of Marine Research*, *51*(2), 237-271.
989 Klunder, M. B., P. Laan, R. Middag, H. J. W. De Baar, and J. C. Van Ooijen (2011), Dissolved
990 iron in the Southern Ocean (Atlantic sector), *Deep Sea Research Part II: Topical Studies in*
991 *Oceanography*, *58*(25), 2678-2694.
992 Kortzinger, A., et al. (2008), Seasonal cycle of O_2 and pCO_2 in the central Labrador Sea:
993 Atmospheric, biological, and physical implications, *Global Biogeochemical Cycles*, *22*(1).
994 doi. 10.1029/2007GB003029
995 Laubscher, R. K., R. Perissinotto, and C. D. McQuaid (1993), Phytoplankton production and
996 biomass at frontal zones in the atlantic sector of the Southern Ocean, *Polar Biology*, *13*(7),
997 471-481.
998 Laws, E. A. (1991), Photosynthetic quotients, new production and net community production in
999 the open ocean, *Deep-Sea Res*, *38*(1), 143-167.
1000 Liang, J. H., C. Deutsch, J. C. McWilliams, B. Baschek, P. P. Sullivan, and D. Chiba (2013),
1001 Parameterizing bubble-mediated air-sea gas exchange and its effect on ocean ventilation,
1002 *Global Biogeochemical Cycles*, *27*(3), 894-905.
1003 Loose, B., W. R. McGillis, P. Schlosser, D. Perovich, and T. Takahashi (2009), Effects of
1004 freezing, growth, and ice cover on gas transport processes in laboratory seawater
1005 experiments, *Geophysical Research Letters*, *36*(5).
1006 Lorbacher, K., D. Dommernget, P.P. Niiler, Köhl A. (2006), Ocean mixed layer depth: A
1007 subsurface proxy of ocean-atmosphere variability, *Journal of Geophysical Research:*
1008 *Oceans*, *111*(C7).

1009 Marinov, I., A. Gnanadesikan, J. R. Toggweiler, and J. L. Sarmiento (2006), The Southern
1010 Ocean biogeochemical divide, *Nature*, *441*(7096), 964-967.
1011 Martinson, D. G., and D. C. McKee (2012), Transport of warm Upper Circumpolar Deep Water
1012 onto the western Antarctic Peninsula continental shelf, *Ocean Sci.*, *8*(4), 433.
1013 McNeil, C., D. Katz, R. Wanninkhof, and B. Johnson (2005), Continuous shipboard sampling of
1014 gas tension, oxygen and nitrogen, *Deep Sea Research Part I: Oceanographic Research*
1015 *Papers*, *52*(9), 1767-1785.
1016 McNeil, C. L., B. D. Johnson, and D. M. Farmer (1995), In situ measurement of dissolved
1017 nitrogen and oxygen in the ocean, *Deep Sea Research Part I: Oceanographic Research*
1018 *Papers*, *42*(5), 819-826.
1019 Mehrbach, C., Culberso.Ch, J. E. Hawley, and R.M. Pytkowic (1973), Measurement of apparent
1020 dissociation constants of carbonic acid in seawater at atmospheric pressure, *Limnology and*
1021 *Oceanography*, *18*(6), 897-907.
1022 Nicholson, D., S. Emerson, and C. C. Eriksen (2008), Net community production in the deep
1023 euphotic zone of the subtropical North Pacific gyre from glider surveys, *Limnology and*
1024 *Oceanography*, *53*(5), 2226.
1025 Nicholson, D., S. Emerson, and C. C. Eriksen (2011), An inverse approach to estimate bubble-
1026 mediated air-sea gas flux from inert gas measurements, *Proceedings on the 6th*
1027 *International Symposium on Gas Transfer at Water Surfaces*, *Kyoto University Press.*
1028 Orsi, A. H., H., T. Whitworth Iii, and W. D. Nowlin Jr (1995), On the meridional extent and
1029 fronts of the Antarctic Circumpolar Current, *Deep Sea Research Part I: Oceanographic*
1030 *Research Papers*, *42*(5), 641-673.
1031 Pierrot, D., E. Lewis, and D. W. R. Wallace (2006), MS Excel program developed for CO2
1032 system calculations, *ORNL/CDIAC-105. Carbon Dioxide Information Analysis Center,*
1033 *Oak Ridge National Laboratory, US Department of Energy, Oak Ridge, Tennessee*.
1034 Planquette, H., R. M. Sherrell, S. Stammerjohn, and M. P. Field (2013), Particulate iron delivery
1035 to the water column of the Amundsen Sea, Antarctica, *Marine Chemistry*, *153*, 15-30.
1036 Reuer, M. K., R. M. Sherrell, S. Stammerjohn, and M. P. Field (2007), New estimates of
1037 Southern Ocean biological production rates from O_2/Ar ratios and the triple isotope
1038 composition of O-2, *Deep-Sea Research Part I-Oceanographic Research Papers*, *54*(6),
1039 951-974.

1040 Rohardt, G., E. Fahrbach, and A. Wisotzki. (2011), Physical oceanography during
1041 POLARSTERN cruise ANT-XXVII/2, *Alfred Wegener Institute, Helmholtz Center for*
1042 *Polar andMarine Research.*, *Pangaea.*
1043 Rubin, S. I., T. Takahashi, D. W. Chipman, and J. G. Goddard (1998), Primary productivity and
1044 nutrient utilization ratios in the Pacific sector of the Southern Ocean based on seasonal
1045 changes in seawater chemistry, *Deep Sea Research Part I: Oceanographic Research*
1046 *Papers*, *45*(8), 1211-1234.
1047 Sarmiento, J. L., and J. R. Toggweiler (1984), A new model for the role of the oceans in
1048 determining atmospheric PCO_2, *Nature*, *308*(5960), 621-624.
1049 Sarmiento, J. L., N. Gruber, M. A. Brzezinski, and J. P. Dunne (2004), High-latitude controls of
1050 thermocline nutrients and low latitude biological productivity, *Nature*, *427*(6969), 56-60.
1051 Sarmiento, J. L., and N. Gruber (2006), Ocean Biogeochemical Dynamics, *Princeton University*
1052 *Press*.
1053 Schlitzer, R. (2002), Carbon export fluxes in the Southern Ocean: results from inverse modeling
1054 and comparison with satellite-based estimates, *Deep-Sea Research Part Ii-Topical Studies*
1055 *in Oceanography*, *49*(9-10), 1623-1644.
1056 Schudlich, R., and S. Emerson (1996), Gas supersaturation in the surface ocean: The roles of
1057 heat flux, gas exchange, and bubbles, *Deep Sea Research Part II: Topical Studies in*
1058 *Oceanography*, *43*(2), 569-589.
1059 Sedwick, P. N., and G. R. DiTullio (1997), Regulation of algal blooms in Antarctic shelf waters
1060 by the release of iron from melting sea ice, *Geophysical Research Letters*, *24*(20), 2515-
1061 2518.
1062 Shadwick, E. H., B. Tilbrook, N. Cassar, T. W. Trull, and S. R. Rintoul (2014), Summertime
1063 physical and biological controls on O2 and CO2 in the Australian Sector of the Southern
1064 Ocean, *Journal of Marine Systems*.
1065 Smith, W. O., and D. M. Nelson (1985), Phytoplankton bloom produced by a receding ice edge
1066 in the Ross Sea - spatial coherence with the density field., *Science*, *227*(4683), 163-166.
1067 Smith, W. O., and L. I. Gordon (1997), Hyperproductivity of the Ross Sea(Antarctica) polynya
1068 during austral spring, *Geophy. Res. Lett.*, *24*(3), 233-236.

1069 Sokolov, S., and S. R. Rintoul (2007), On the relationship between fronts of the Antarctic
1070 Circumpolar Current and surface chlorophyll concentrations in the Southern Ocean,
1071 *Journal of Geophysical Research-Oceans*, *112*(C7).
1072 Sokolov, S. (2008), Chlorophyll blooms in the Antarctic Zone south of Australia and New
1073 Zealand in reference to the Antarctic Circumpolar Current fronts and sea ice forcing,
1074 *Journal of Geophysical Research-Oceans*, *113*(C3).
1075 Spreen, G., L. Kaleschke, and G. Heygster (2008), Sea ice remote sensing using AMSRE 89
1076 GHz channels, *Journal of Geophysical Research: Oceans*, *113*(C2).
1077 Stanley, R. H. R., W. J. Jenkins, D. E. Lott, and S. C. Doney (2009), Noble gas constraints on
1078 air-sea gas exchange and bubble fluxes, *Journal of Geophysical Research-Oceans*, *114*.
1079 Sweeney, C. (2003), The annual cycle of surface CO 2 and O 2 in the Ross Sea: A model for gas
1080 exchange on the continental shelves of Antarctica, *Biogeochemistry of the Ross Sea,*
1081 *Antarctic Research Series (78), edited GR DiTullio and RB Dunbar*, 295-312.
1082 Sweeney, C., E. Gloor, A. R. Jacobson, R. M. Key, G. McKinley, J. L. Sarmiento, and R.
1083 Wanninkhof (2007), Constraining global air-sea gas exchange for CO2 with recent bomb
1084 C-14 measurements, *Global Biogeochemical Cycles*, *21*(2).
1085 Takahashi, T., S. C. Sutherland, C. Sweeney, A. Poisson, N. Metzl, B. Tilbrook, N. Bates, R.
1086 Wanninkhof, R. A. Feely, C. Sabine, J. Olafsson, and Y. Nojiri (2002), Global sea-air CO_2
1087 flux based on climatological surface ocean pCO_2, and seasonal biological and temperature
1088 effects, *Deep-Sea Research Part II-Topical Studies in Oceanography*, *49*(9-10), 1601-
1089 1622.
1090 Takahashi, T., S. C. Sutherland, R. Wanninkhof, C. Sweeney, R. A. Feely, D. W. Chipman, B.
1091 Hales, G. Friederich, F. Chavez, and C. Sabine (2009), Climatological mean and decadal
1092 change in surface ocean pCO_2 , and net sea-air CO_2 flux over the global oceans, *Deep Sea*
1093 *Research Part II: Topical Studies in Oceanography*, *56*(8-10), 554-577.
1094 Tortell, P. D., and M. C. Long (2009), Spatial and temporal variability of biogenic gases during
1095 the Southern Ocean spring bloom, *Geophysical Research Letters*, *36*.
1096 Tortell, P. D., C. Guéguen, M. C. Long, C. D. Payne, P. Lee, and G. R. DiTullio (2011), Spatial
1097 variability and temporal dynamics of surface water pCO2, DO2/Ar and dimethylsulfide in
1098 the Ross Sea, Antarctica, *Deep Sea Research Part I: Oceanographic Research Papers*,
1099 *58*(3), 241-259.

Tortell, P. D., M. C. Long, C. D. Payne, A. C. Alderkamp, P. Dutrieux, and K. R. Arrigo (2012), Spatial distribution of pCO_2, $\Delta O_2/Ar$ and dimethylsulfide (DMS) in polynya waters and the sea ice zone of the Amundsen Sea, Antarctica, *Deep Sea Research Part II: Topical Studies in Oceanography*.

Tortell, P. D., E. C. Asher, H. Ducklow, J. A. L. Goldman, J. W. H. Dacey, J. J. Grzymski, J. N. Young, S. A. Kranz, K. S. Bernard, and F. M. M. Morel (2014), Metabolic balance of coastal Antarctic waters revealed by autonomous pCO_2 and $\Delta O_2/Ar$ measurements., *Geophysical Research Letters*.

Trull, T. W., S. G. Bray, S. J. Manganini, S. Honjo, and R. Francois (2001), Moored sediment trap measurements of carbon export in the Subantarctic and Polar Frontal Zones of the Southern Ocean, south of Australia, *Journal of Geophysical Research: Oceans* 106 (C12), 31489-31509.

Vagle, S., C. McNeil, and N. Steiner (2010), Upper ocean bubble measurements from the NE Pacific and estimates of their role in air-sea gas transfer of the weakly soluble gases nitrogen and oxygen, *Journal of Geophysical Research: Oceans (1978â€“2012)*, *115*(C12).

Waters, K. J., and R. C. Smith (1992), Palmer LTER: A sampling grid for the Palmer LTER program, *Antarctic Journal of the United States*, *27*(5), 236-239.

Weeding, B., and T. W. Trull (2014), Hourly oxygen and total gas tension measurements at the Southern Ocean Time Series site reveal winter ventilation and spring net community production, *Journal of Geophysical Research: Oceans*, *119*(1), 348-358.

Weiss, R. F. (1974), Carbon dioxide in water and seawater: the solubility of a non-ideal gas, *Marine Chemistry*, *2*(3), 203-215.

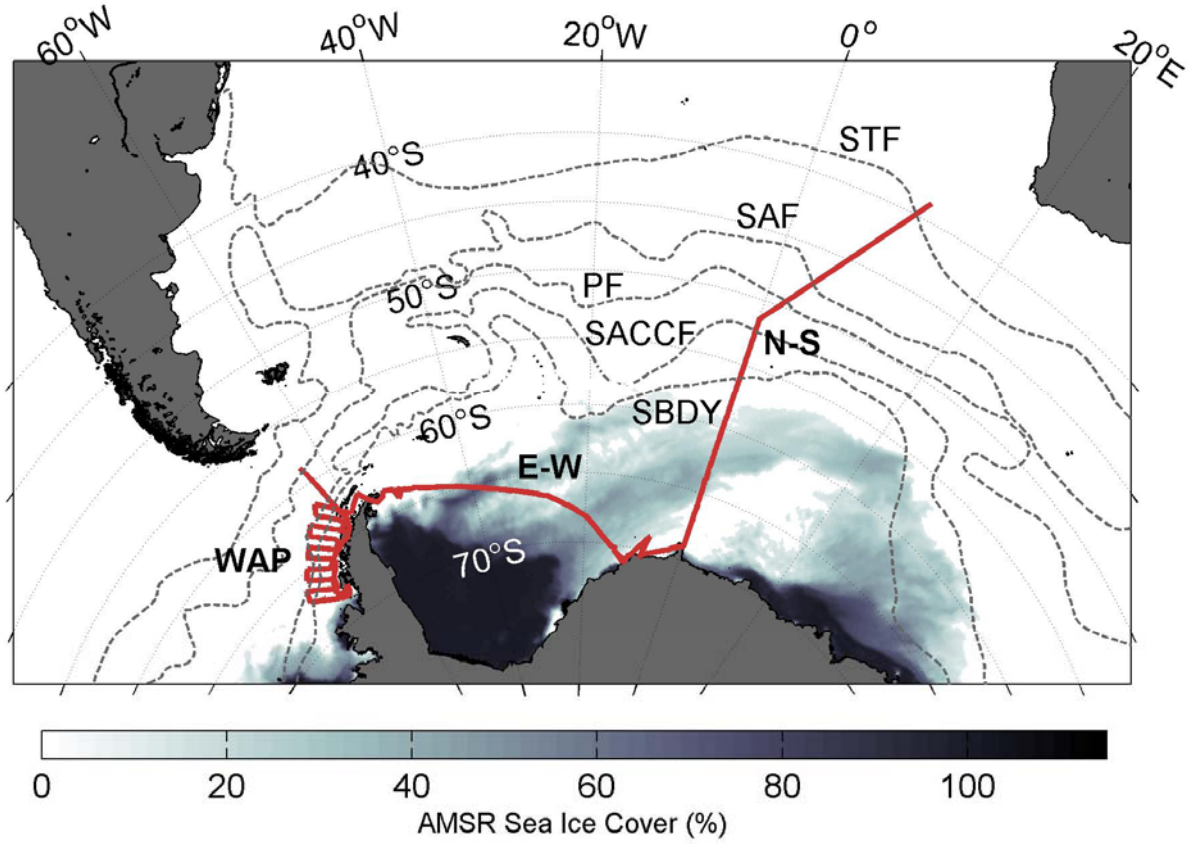
60°W
40°W
20°W
0°
20°E
40°S
STF
SAF
50°S
PF
SACCF
N-S
60°S
SBDY
E-W
WAP
70°S
0
20
40
60
80
100
AMSR Sea Ice Cover (%)

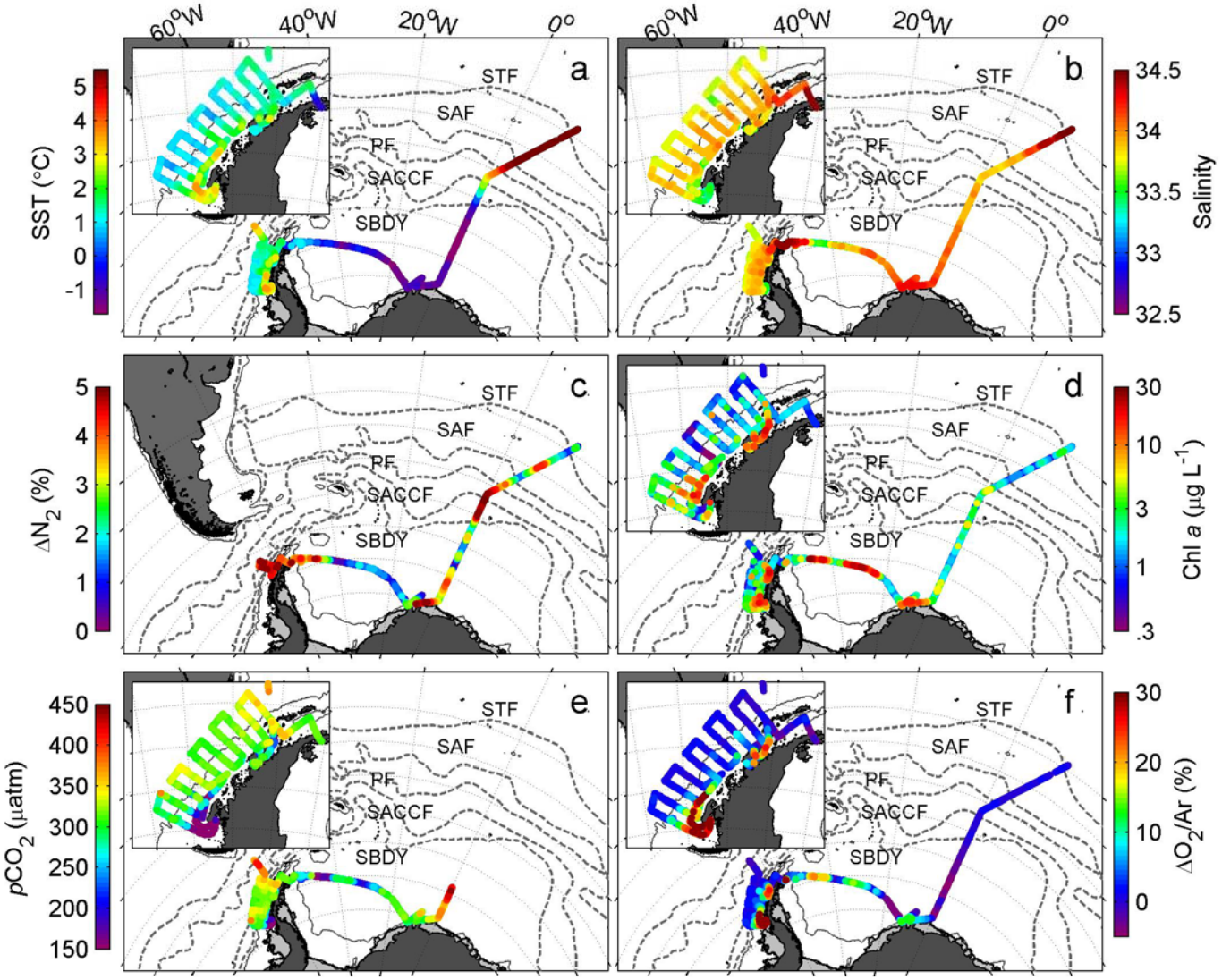
60°W
40°W
20°W
0°
a
b
c
d
e
f
STF
SAF
PF
SACCF
SBDY
SST (°C)
5
4
3
2
1
0
-1
Salinity
34.5
34
33.5
33
32.5
ΔN2 (%)
5
4
3
2
1
0
Chl a (μg L-1)
30
10
3
1
.3
pCO2 (μatm)
450
400
350
300
250
200
150
ΔO2/Ar (%)
30
20
10
0

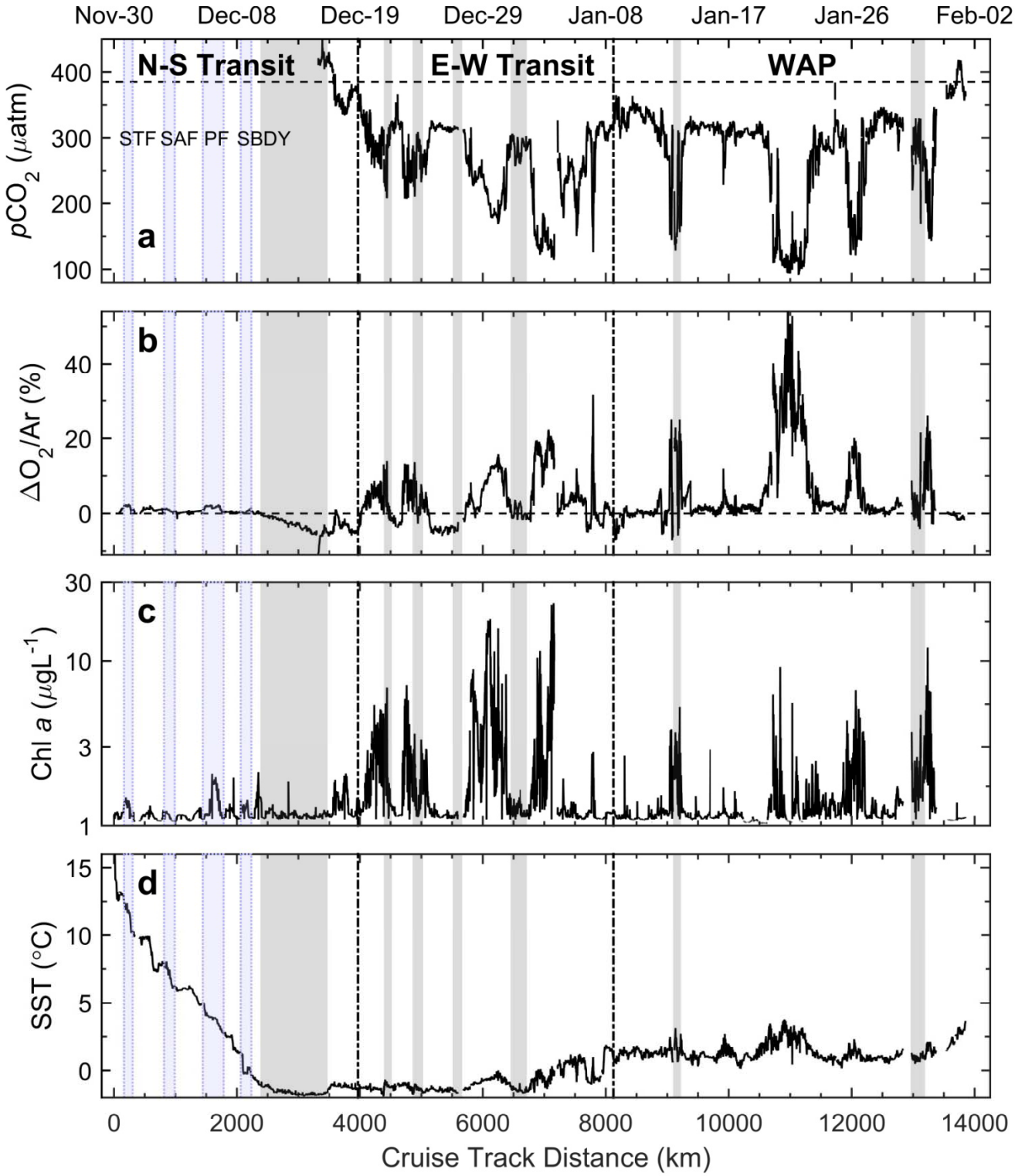
Nov-30
Dec-08
Dec-19
Dec-29
Jan-08
Jan-17
Jan-26
Feb-02
N-S Transit
E-W Transit
WAP
STF SAF PF SBDY
a
b
c
d
pCO2 (μatm)
ΔO2/Ar (%)
Chl a (μgL-1)
SST (°C)
Cruise Track Distance (km)

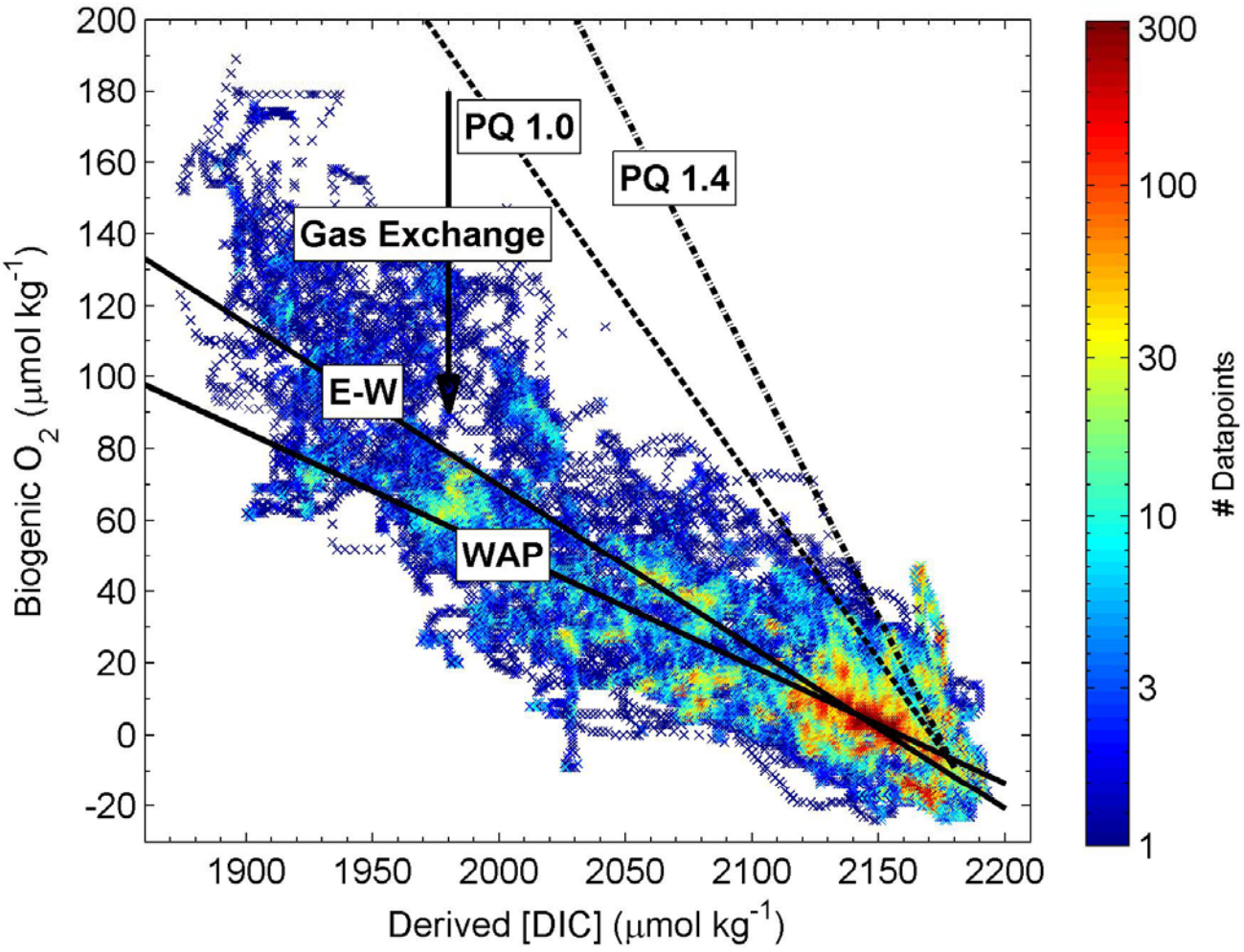
PQ 1.0
PQ 1.4
Gas Exchange
E-W
WAP
Biogenic O_2 (μmol kg^{-1})
Derived [DIC] (μmol kg^{-1})
Datapoints
200
180
160
140
120
100
80
60
40
20
0
-20
1900
1950
2000
2050
2100
2150
2200
300
100
30
10
3
1

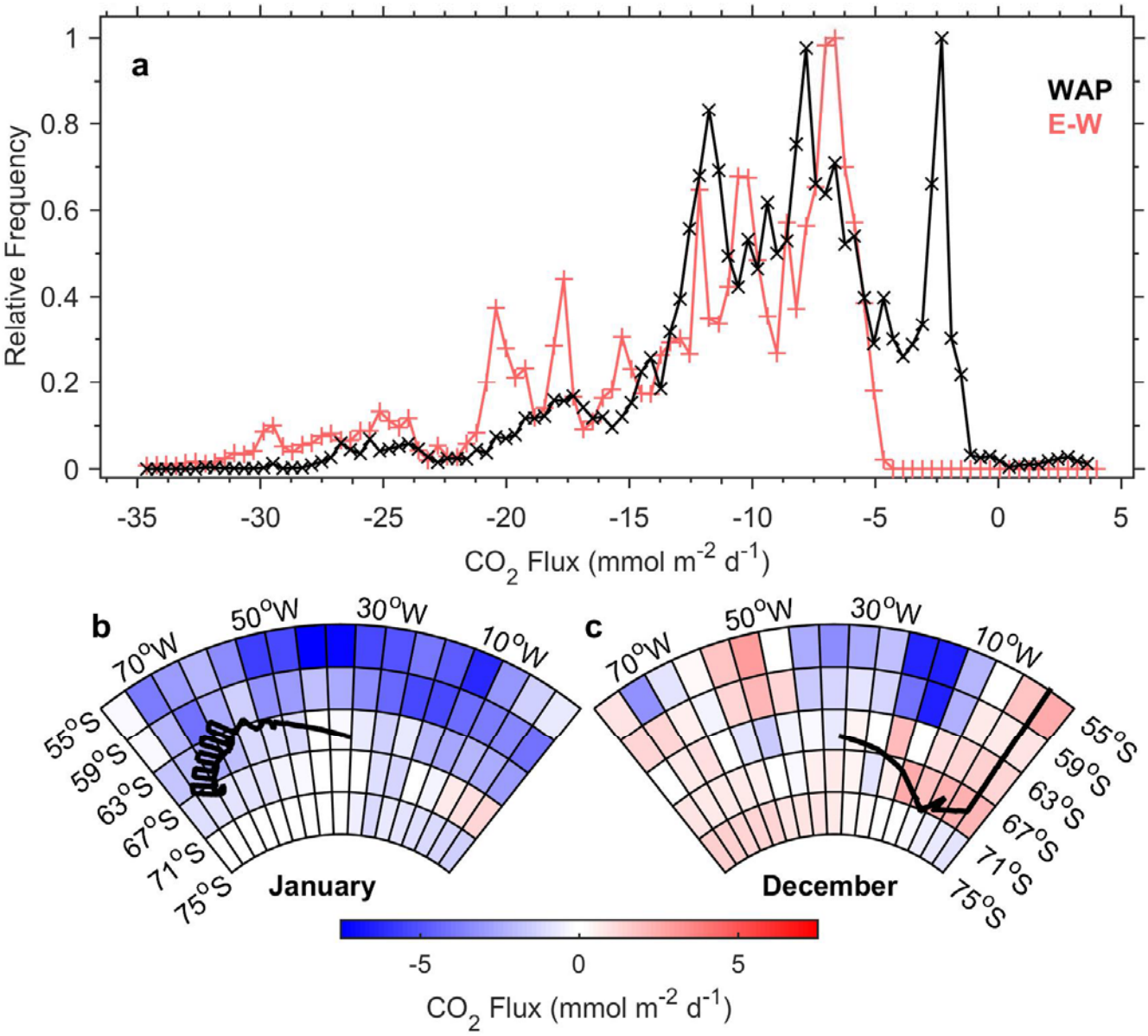
a
WAP
E-W
Relative Frequency
1
0.8
0.6
0.4
0.2
0
-35
-30
-25
-20
-15
-10
-5
0
5
CO2 Flux (mmol m-2 d-1)
b
c
70°W
50°W
30°W
10°W
55°S
59°S
63°S
67°S
71°S
75°S
January
December
-5
0
5
CO2 Flux (mmol m-2 d-1)

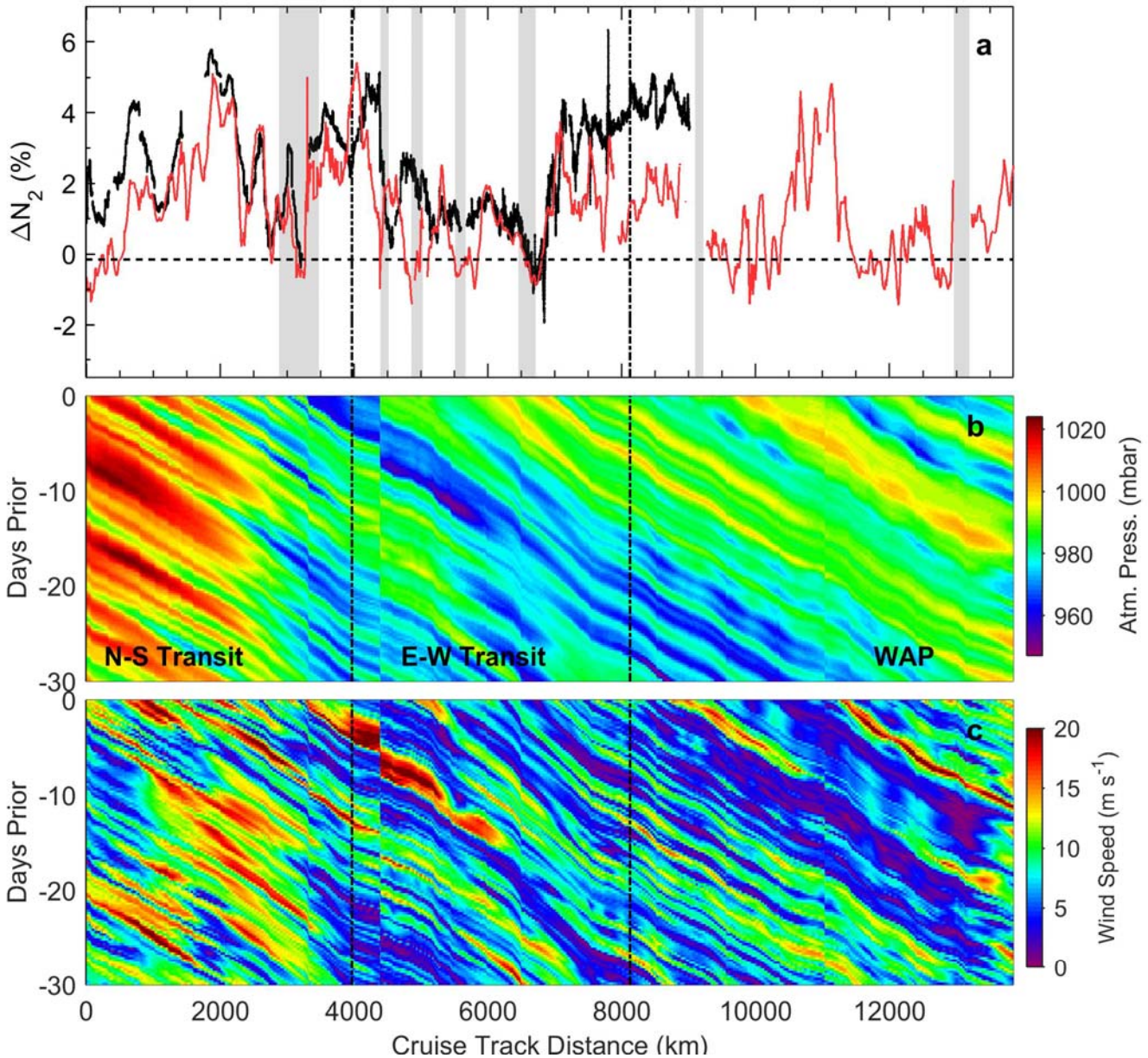
a
b
c
ΔN_2 (%)
6
4
2
0
-2
Days Prior
0
-10
-20
-30
N-S Transit
E-W Transit
WAP
1020
1000
980
960
Atm. Press. (mbar)
20
15
10
5
0
Wind Speed (m s^{-1})
0
2000
4000
6000
8000
10000
12000
Cruise Track Distance (km)

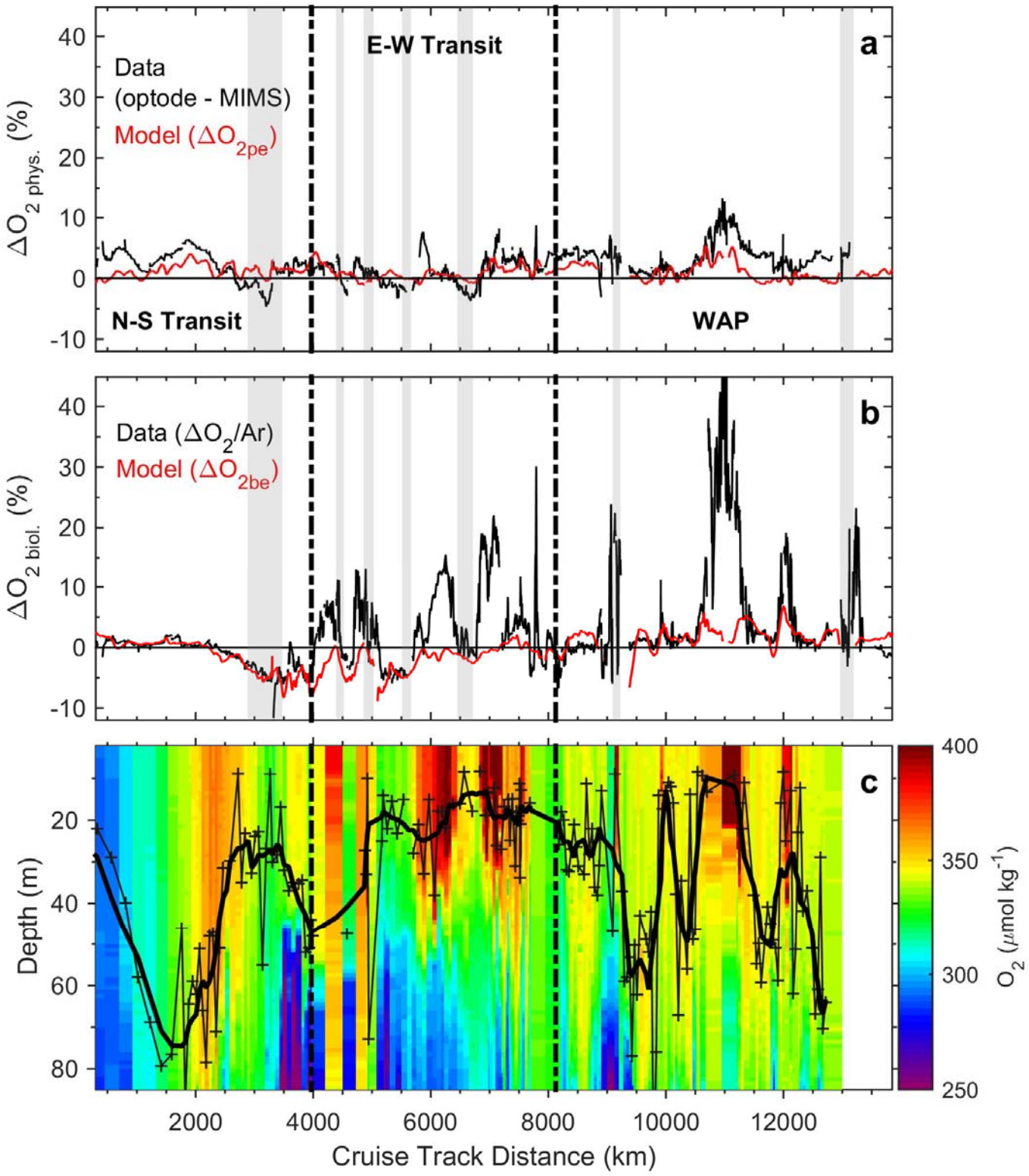
a
E-W Transit
Data
(optode - MIMS)
Model (ΔO2pe)
N-S Transit
WAP
ΔO2 phys. (%)
40
30
20
10
0
-10
b
Data (ΔO2/Ar)
Model (ΔO2be)
ΔO2 biol. (%)
c
Depth (m)
20
40
60
80
2000
4000
6000
8000
10000
12000
Cruise Track Distance (km)
400
350
300
250
O2 (μmol kg-1)

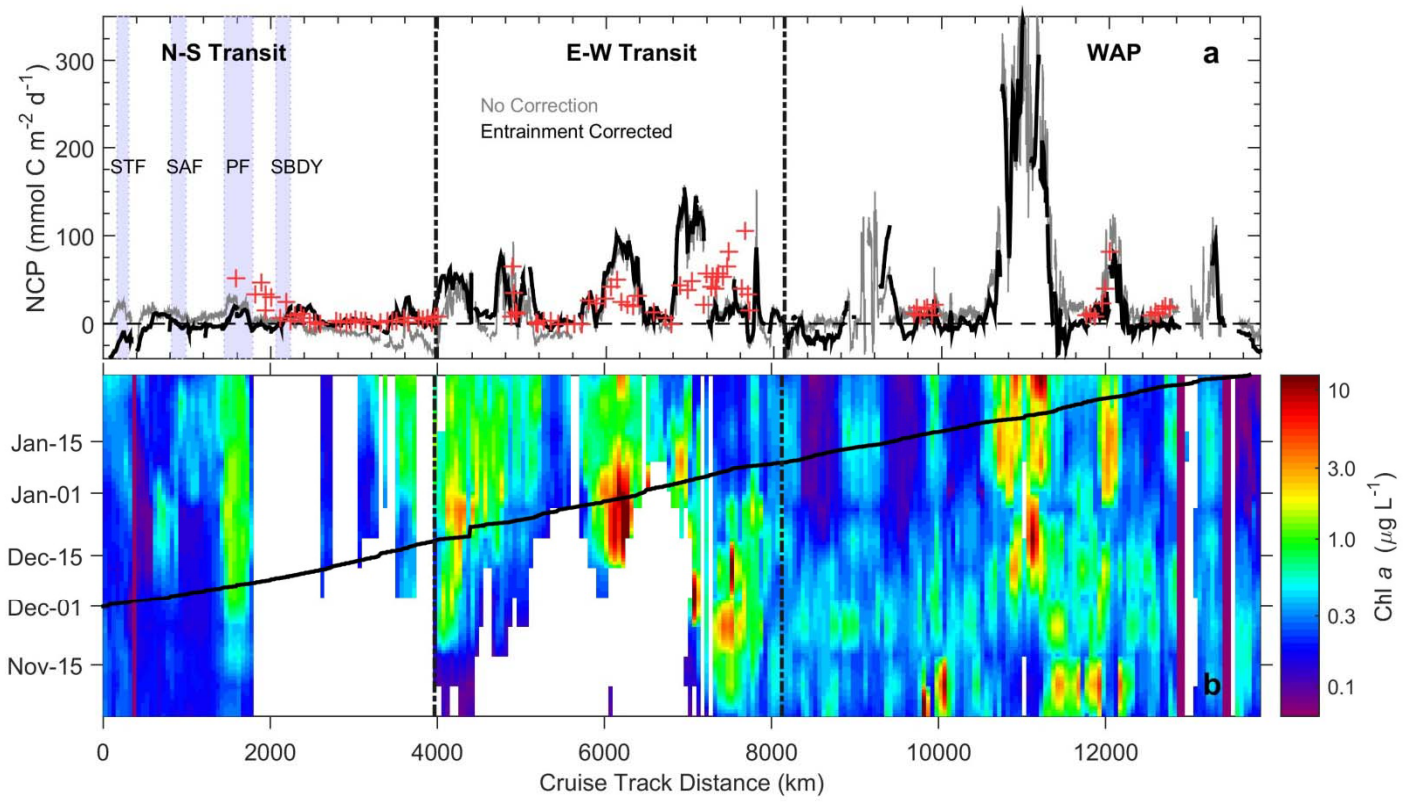
N-S Transit
E-W Transit
WAP
a
No Correction
Entrainment Corrected
STF
SAF
PF
SBDY
NCP (mmol C m-2 d-1)
300
200
100
0
Jan-15
Jan-01
Dec-15
Dec-01
Nov-15
b
10
3.0
1.0
0.3
0.1
Chl a (μg L-1)
0
2000
4000
6000
8000
10000
12000
Cruise Track Distance (km)

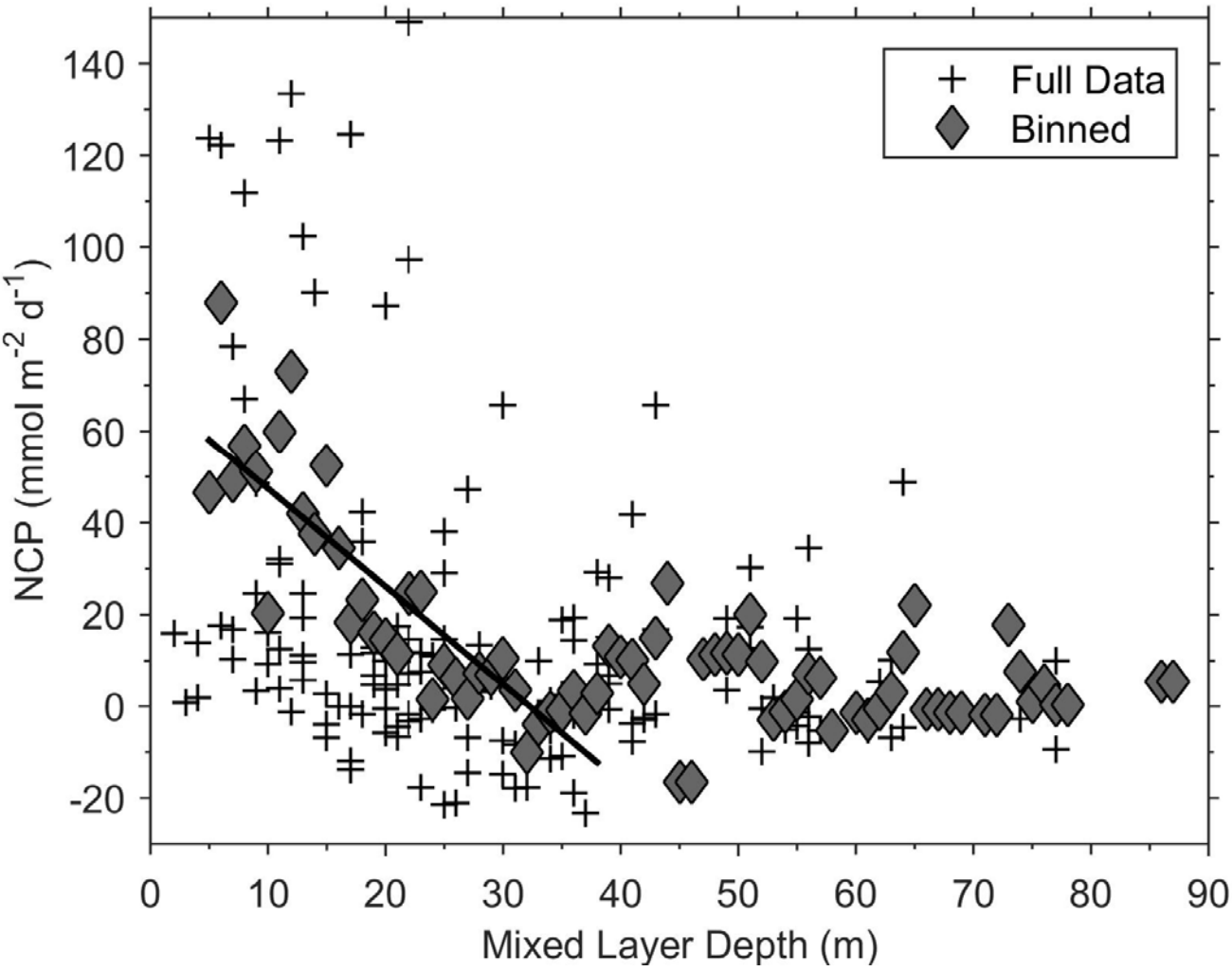
Full Data
Binned
NCP (mmol m-2 d-1)
Mixed Layer Depth (m)
140
120
100
80
60
40
20
0
-20
0
10
20
30
40
50
60
70
80
90